The Carnegie-Irvine Galaxy Survey. IX. Classification of Bulge Types and Statistical Properties of Pseudo Bulges

Hua Gao (高桦)[1,2] , Luis C. Ho[2,1] , Aaron J. Barth[3] , and Zhao-Yu Li[4]

[1] Department of Astronomy, School of Physics, Peking University, Beijing 100871, People's Republic of China; hgao.astro@gmail.com
[2] Kavli Institute for Astronomy and Astrophysics, Peking University, Beijing 100871, People's Republic of China
[3] Department of Physics and Astronomy, University of California at Irvine, 4129 Frederick Reines Hall, Irvine, CA 92697-4575, USA
[4] Department of Astronomy, Shanghai Jiao Tong University, Shanghai 200240, People's Republic of China

Abstract

We study the statistical properties of 320 bulges of disk galaxies in the Carnegie-Irvine Galaxy Survey, using robust structural parameters of galaxies derived from image fitting. We apply the Kormendy relation to classify classical and pseudo bulges and characterize the bulge dichotomy with respect to the structural properties of the bulges and the physical properties of the host galaxies. We confirm previous findings that pseudo bulges on average have smaller Sérsic indices, lower bulge-to-total ratios, and fainter surface brightnesses than classical bulges. Our sizable sample statistically shows that pseudo bulges are more intrinsically flattened than classical bulges. Pseudo bulges are most frequent (incidence $\gtrsim 80\%$) in late-type spirals (later than Sc). Our measurements support the picture in which pseudo bulges arose from star formation induced by inflowing gas, while classical bulges were born out of violent processes such as mergers and coalescence of clumps. We reveal differences with the literature that warrant attention: (1) the bimodal distribution of Sérsic indices presented by previous studies is not reproduced in our study; (2) classical and pseudo bulges have similar relative bulge sizes; and (3) the pseudo bulge fraction is considerably smaller in early-type disks than reported in previous studies based on one-dimensional surface brightness profile fitting. We attribute these differences to our improved image quality, more robust bulge-to-disk decomposition technique, and to the different classification criteria that we applied. Moreover, we find that barred galaxies do not host more pseudo bulges or more prominent pseudo bulges than unbarred galaxies. Various implications of these findings are discussed.

Unified Astronomy Thesaurus concepts: Galaxy bulges (578); Galaxy structure (622); Galaxy photometry (611); Disk galaxies (391); Elliptical galaxies (456); Galaxy evolution (594)

Supporting material: figure set, machine-readable table

1. Introduction

The Fundamental Plane (FP) of elliptical galaxies was first established in the 1980s (Djorgovski & Davis 1987; Dressler et al. 1987) and has long proved to be a useful tool for estimating distances and studying the formation and evolution of these systems (Dressler et al. 1987; Faber et al. 1987; Djorgovski et al. 1988; Lynden-Bell et al. 1988; D'Onofrio et al. 2013, 2017; Zhang & Zaritsky 2016). The FP is a three-parameter correlation of the galaxy half-light (effective) radius r_e, central velocity dispersion σ_0, and average effective surface brightness $\langle \mu_e \rangle$:

$$\log r_e = a \log \sigma_0 + b \langle \mu_e \rangle + c. \qquad (1)$$

At the most basic level, the physical root of the relation is the virial theorem (Djorgovski & Davis 1987; Djorgovski et al. 1988; Kormendy & Djorgovski 1989),

$$\frac{GM}{r_g} \sim \langle v^2 \rangle, \qquad (2)$$

where M is the total mass, r_g is the gravitational radius, and $\langle v^2 \rangle$ is the mean square of stellar velocity (Binney & Tremaine 2008). To translate the physical parameters in the virial theorem into observables, one has to make assumptions about the density, kinematic structure, and dynamical mass-to-light ratio (M/L) of the galaxies. Rewriting Equation (2) to follow

the formulation of Equation (1), we have

$$\log r_e = 2 \log \sigma_0 + 0.4 \langle \mu_e \rangle + \log \left[k \left(\frac{M}{L} \right)^{-1} \right] + C, \qquad (3)$$

where k accounts for the projection effect and intrinsic density and kinematic structure of the galaxies. The observed coefficients a and b in Equation (1) generally deviate from 2 and 0.4, respectively, which is commonly termed the tilt of the FP with respect to the virial plane. The heterogeneity of density and kinematic structures and dynamical mass-to-light ratios of ellipticals may contribute to the tilt, although which factor plays a dominant role is still debated. Ellipticals have long been approximated as homologous stellar systems, so the contribution of heterogeneity of their structures to the tilt was often neglected. Assuming that ellipticals have homologous density and kinematics, some authors found $M/L \sim M^{0.2}$ (Djorgovski 1987; Faber et al. 1987; Pahre et al. 1998; Treu et al. 2005). Factors that may lead to variations of dynamical mass-to-light ratio include metallicity (e.g., Djorgovski & Davis 1987), initial mass function (e.g., Renzini & Ciotti 1993; Kroupa 2001; Cappellari et al. 2012), and dark matter (e.g., Ciotti et al. 1996; Cappellari et al. 2006, 2013b). In addition to these possibilities, the heterogeneity of density and kinematics of ellipticals may also tilt the FP. Ellipticals are now known to be not strictly homologous in terms of light profile (Nieto et al. 1991;

Lauer et al. 1995, 2005, 2007; Kormendy et al. 1996, 2009; Bertin et al. 2002) and kinematic structure (Illingworth 1977; Davies et al. 1983; Bender 1987, 1988; Emsellem et al. 2011). Busarello et al. (1997) stressed the importance of kinematic heterogeneity in causing the tilt, and that structural heterogeneity and stellar population effects play a minor role. In contrast, D'Onofrio et al. (2013) concluded that the tilt is mainly affected by structural heterogeneity. However, Ciotti et al. (1996) and Cappellari et al. (2006, 2013b) disagreed. In addition to the tilt, studying the residuals of the FP provides insights into and constrains the regularity or stochasticity of the formation and evolution of elliptical galaxies (Renzini & Ciotti 1993; Borriello et al. 2003; D'Onofrio et al. 2013, 2017).

Even though ellipticals are not a strictly homologous population, the tightness of the FP implies their highly regulated formation and evolution pathways, especially when compared with other stellar systems. For example, star-forming disks on the other end of the Hubble sequence differ from the ellipticals in every aforementioned aspect that could cause the tilt and amplify the scatter of the scaling relations. Hence, the FP relation is useful to distinguish stellar systems of distinct physical nature. One notably successful example in application of the FP projections and their variants was the discovery of the dichotomy between elliptical and spheroidal galaxies (Kormendy 1985, 1987; Bender et al. 1992; Binggeli 1994). These authors showed that spheroidal galaxies form a sequence distinct from that of ellipticals in the core parameter correlations (i.e., central surface brightness and core radius—a projection of the core FP; see Kormendy 1985, 1987; Lauer 1985; Binggeli 1994) and in the κ formulation of the FP (Bender et al. 1992). Surprisingly, in these parameter spaces, spheroidals occupy a locus that overlaps with the disks of spiral galaxies. The dichotomy between slow-rotator and fast-rotator ellipticals (e.g., Illingworth 1977; Davies et al. 1983; Emsellem et al. 2011) is also another manifestation of the application of the core parameter correlations, but it is much less obvious than the elliptical versus spheroidal dichotomy (Faber et al. 1997).

Since the seminal work of van den Bergh (1976), Combes & Sanders (1981), Gallagher et al. (1982), Kormendy (1982a, 1982b, 1993), Kormendy & Illingworth (1982, 1983), Pfenniger (1984, 1985), Combes et al. (1990), and Pfenniger & Norman (1990), two classes of bulges are recognized in disk (S0 and spiral) galaxies. Classical bulges have similar observational properties as ellipticals (Faber 1977; Gott 1977; Renzini 1999) and are therefore considered to form out of rapid, violent processes such as mergers and coalescence of clumps (Toomre 1977; Bournaud 2016). They follow the scaling relations defined by ellipticals (Kormendy 1985, 1987; Bender et al. 1992). On the other hand, pseudo bulges are more likely central miniature disks embedded in the large-scale disks. They have younger, more composite stellar populations, more flattened stellar light distribution, and more rotation-dominated kinematics than classical bulges (e.g., Wyse et al. 1997; Kormendy & Kennicutt 2004; Fisher & Drory 2016; Kormendy 2016). In contrast with the violent origin of classical bulges, pseudo bulges are deemed to form out of redistributed disk material by gradual, secular processes facilitated by non-axisymmetry in the galaxy potential (Combes & Sanders 1981; Kormendy 1981, 1982b; Pfenniger & Norman 1990; Sellwood & Wilkinson 1993). Pseudo bulges are found to be low surface brightness outliers in the Kormendy (1977) relation—the correlation between surface brightness and effective radius of ellipticals, which constitutes the photometric

projection of the FP (e.g., Carollo 1999; Gadotti 2009; Fisher & Drory 2010; Laurikainen et al. 2010; but see Kim et al. 2017; Kim & Ho 2019; Zhao et al. 2019) for the case of active galaxies). The dichotomy between classical and pseudo bulges is the main subject of this paper.

In addition to using the Kormendy relation, there are alternative ways to distinguish classical bulges from pseudo bulges. For example, the Sérsic (1968) index n is widely used to separate the two categories of bulges. Based on the bimodal distribution of n found by Fisher & Drory (2008, 2016), these authors proposed that pseudo bulges be defined by $n < 2$. The bulge type is statistically linked with the Hubble type (pseudo bulges occur most frequently in spirals of type Sbc and later (Kormendy & Kennicutt 2004, and references therein), and thus bulge-to-total ratio (B/T), but the correspondence is imperfect because the correlation between Hubble type and B/T has large scatter (e.g., Kent 1985; Simien & de Vaucouleurs 1986; de Jong 1996; Grosbøl et al. 2004; Laurikainen et al. 2007, 2010; Weinzirl et al. 2009; Méndez-Abreu et al. 2017; Gao et al. 2019). While a low B/T does not guarantee a pseudo bulge, pseudo bulges are generally found in galaxies with $B/T \lesssim 0.35$; if $B/T \gtrsim 0.5$, the bulge is very likely classical (Kormendy & Ho 2013; Kormendy 2016). The bulge size was used in conjunction with B/T to classify bulges in Allen et al. (2006). Central morphological features, such as nuclear bars, rings, or spirals that are indicative of kinematically cold bulges, boxy/peanut bulges that are actually thickened bars, or apparent flattenings similar to those of disks are useful diagnostics to recognize pseudo bulges (e.g., Kormendy & Kennicutt 2004; Fisher & Drory 2008, 2010; Fisher et al. 2009; Kormendy & Ho 2013; Kormendy 2016). Stellar kinematics provide perhaps the cleanest diagnostic, but they are not readily available for large samples. Pseudo bulges are characterized by their higher degree of rotation relative to random motion (Kormendy & Illingworth 1982; Kormendy 1982a), stand out as low-σ outliers in the Faber & Jackson (1976) relation (Kormendy & Illingworth 1983; Kormendy & Kennicutt 2004), and have flat central σ profiles (Fisher & Drory 2016). Some extreme cases even show σ drops at the center. Vigorous star formation and young stellar populations, if not induced by mergers, are signposts of ongoing growth of pseudo bulges (Kormendy & Kennicutt 2004; Fisher et al. 2009; Fisher & Drory 2016). For complete reviews of the observational criteria to classify classical and pseudo bulges, see Kormendy & Kennicutt (2004), the supplemental material of Kormendy & Ho (2013), Fisher & Drory (2016), and Kormendy (2016). Unfortunately, these many criteria do not necessarily produce consistent results. Robust classifications can be achieved by applying as many criteria as possible. To resolve the ambiguity, Neumann et al. (2017) performed a comprehensive comparison among the commonly adopted criteria Sérsic index, concentration index, the Kormendy relation, and the inner slope of radial velocity dispersion profile. They found that the Kormendy relation is the best single criterion, as it is able to recover 39 out of 40 "safe" classifications, where safe classifications were defined as consistent classifications that resulted from at least three out of the four criteria.

In order to characterize the bulge dichotomy in the local Universe, we consistently apply the Kormendy relation to classify classical and pseudo bulges because it has a strong physical basis and provides the best agreement with classifications based on multiple criteria. We do not consider the full FP because stellar central velocity dispersions are not available for

a significant fraction of the spiral galaxies in our sample. We use the robust structural parameters derived in Gao et al. (2019). The remainder of this paper is devoted to introducing the Carnegie-Irvine Galaxy Survey (CGS; Ho et al. 2011), measuring the Kormendy relation of CGS ellipticals and bulges, classifying classical and pseudo bulges, studying their statistical properties, and discussing implications on their respective formation and evolution paths.

2. Sample and Data

The CGS sample is defined by $B_T \leqslant 12.9$ mag and $\delta < 0°$, without any reference to morphology, size, or environment. Details of the observations and data reduction are given in Ho et al. (2011) and Li et al. (2011), and are not repeated here. In this study, we mainly use products from the R-band images. The majority of the images are of high quality in terms of field of view ($8'9 \times 8'9$), median seeing ($1''01$), and median surface brightness depth (26.4 mag arcsec^{-2}).

In this paper, we make use of all the successfully decomposed disk galaxies presented in Gao et al. (2019). The CGS disk galaxy sample for bulge-to-disk decomposition is restricted to the subset of galaxies with morphological type index $-3 \leqslant T \leqslant 9.5$ and inclination angle $i \leqslant 70°$. After complementing the sample with a handful of misclassified ellipticals and removing objects whose decomposition was unsuccessful, the final sample consists of 320 S0s and spirals. Basic properties of the sample are discussed in detail in Gao et al. (2019) and are not repeated here. Below we briefly describe the decomposition strategy; we refer readers to Section 3 of Gao et al. (2019) for full details of the decomposition. We performed multicomponent decomposition of the R-band images to derive accurate bulge structural parameters, following closely the technique described in Gao & Ho (2017) and Gao et al. (2018). In addition to bulges and disks, we successfully modeled nuclei, bars, disk breaks, nuclear or inner lenses, and inner rings. Our modeling strategy treats nuclear rings and nuclear bars as part of the bulge component, while other features such as spiral arms, outer lenses, and outer rings were omitted from the fits because they are not crucial for accurate bulge measurements according to the experiments in Gao & Ho (2017). The error budget of the bulge parameters includes the uncertainties from sky level measurements and model assumptions.

In addition to the disk galaxy sample, we perform single-Sérsic fits to 83 ellipticals to measure their structural parameters in the R band (Appendix). The CGS elliptical sample is drawn from Huang et al. (2013a). We remove misclassified ellipticals that have since been classified as S0s in Gao et al. (2018). Although Huang et al. (2013a) promoted the three-component nature of ellipticals, single-Sérsic fits suffice for our purpose of deriving global structural parameters for reference comparison with the bulges on the FP correlations. The uncertainties of the structural parameters stem from the uncertainties in sky subtraction. We estimate the uncertainties in a manner consistent with the bulge measurements. Namely, we measure the sky-induced uncertainties as variations of the best-fit parameters when perturbing the sky levels around $\pm 1\sigma_{sky}$ of the measured sky levels, where uncertainties of the sky level σ_{sky} are measured as the root-mean square of the residuals determined from randomly placed boxes in the sky-dominated region of the sky-subtracted data image (see Appendix B of Gao & Ho 2017 for details). Considering that

ellipticals are more extended than disk galaxies and a single-Sérsic function cannot accurately describe their light profiles across a large dynamical range in radius, we strive to avoid introducing model-induced uncertainties to sky level measurements, which in return may induce errors in Sérsic index measurements. Therefore, instead of simultaneously fitting the sky with the galaxy, as was done for the disk galaxies, we measure the sky level using the direct approach described in Gao & Ho (2017; their Appendix B.1) and subtract it before performing the fits.

3. Results

3.1. The Kormendy Relation of Ellipticals

We derive the Kormendy relation of the ellipticals by minimizing the χ^2, defined as

$$\chi^2 = \sum_{i=1}^{N} \frac{(\langle \mu_{e,i} \rangle - \alpha \log r_{e,i} - \beta)^2}{\xi_{\langle \mu_{e,i} \rangle}^2 + \alpha^2 \xi_{\log r_{e,i}}^2}, \qquad (4)$$

where α and β are the coefficients of the Kormendy relation $\langle \mu_e \rangle = \alpha \log r_e + \beta$ and ξ denotes the uncertainties. The best-fit relation is

$$\langle \mu_e \rangle = (2.38 \pm 0.07) \log r_e + (17.86 \pm 0.04), \qquad (5)$$

with a scatter of 0.42 dex in $\langle \mu_e \rangle$. We correct $\langle \mu_e \rangle$ for Galactic extinction following Ho et al. (2011) and Li et al. (2011).

The best-fit relation is shown in Figure 1, with the bulges of the disk galaxies overlaid. It is immediately apparent that some of the bulges overlap with and continuously extend the high-$\langle \mu_e \rangle$, low-r_e end of the Kormendy relation (the open blue stars), while others (the filled stars) scatter to low values of $\langle \mu_e \rangle$ at fixed r_e. We classify as pseudo bulges those that scatter more than 3σ below the best-fit Kormendy relation of ellipticals and the rest as classical bulges. Namely, pseudo bulges satisfy

$$\langle \mu_e \rangle > 2.38 \log r_e + 19.12, \qquad (6)$$

where $\langle \mu_e \rangle$ and r_e are measured in the R band and r_e is in units of kpc. This relation can be translated into other photometric bands using standard colors of ellipticals from Fukugita et al. (1995). This yields 101 pseudo bulges. Interestingly, only one of the pseudo bulges resides in an S0 galaxy—NGC 4802. Its bulge is dusty but overall blue, signaling recent star formation.

3.2. Classical Bulges Are Not Necessarily Prominent

Figure 2 shows the distribution of B/T in the Kormendy relation (panel b). To mitigate the effects of object overlay, we present a version smoothed by locally weighted regression (LOESS; Cleveland & Devlin 1988)[5] to highlight the general trend (panel c). We find that bulges with constant B/T approximately follow the lines of constant bulge luminosity, although, as expected, considerable curvature is observed, considering that the host galaxies of pseudo bulges are generally less massive and less luminous. We find that along the direction of the Kormendy relation, bulges form a sequence

---

[5] We adopt the implementation of the two-dimensional LOESS method by Cappellari et al. (2013a), who provide the code in http://purl.org/cappellari/idl.
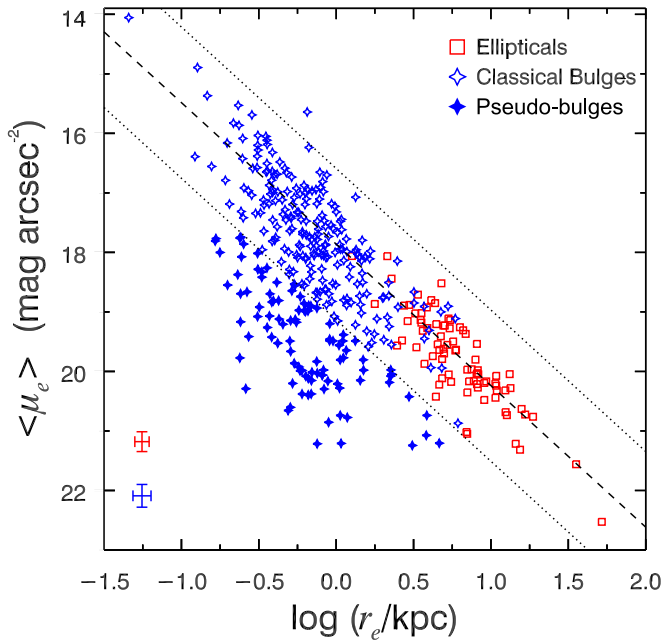
Figure 1. The Kormendy relation of CGS ellipticals and bulges. The best-fit relation and its 3σ boundary of the ellipticals are indicated by the short-dashed lines and dotted lines, respectively. Typical uncertainties are illustrated in the bottom left corner. Blue filled stars represent pseudo bulges that are 3σ low surface brightness outliers from the best-fit relation of the ellipticals (red squares). The other bulges (blue open stars) are designated classical bulges.

of increasing B/T, from small r_e to large r_e. This again reinforces the point that both classical and pseudo bulges can have small and large B/T, even if on average classical bulges have larger B/T.

Pseudo bulges are generally weak, with 78% of them having $B/T < 0.1$ (Figure 2(d)). Meanwhile, classical bulges are not always strong; 26% of them have $B/T < 0.1$. The distributions of B/T for classical and pseudo bulges significantly overlap. The mean B/T of classical bulges is 0.21, not dramatically larger than that of pseudo bulges ($\langle B/T \rangle = 0.08$). Fisher & Drory (2008, hereafter FD08) and Gadotti (2009, hereafter G09) also see such an overlap, but in general, their values of B/T, both of classical and pseudo bulges, are significantly larger than ours (Figure 3). This systematic difference repeatedly shows up when we compare bulge properties derived from two-dimensional (2D) image fitting and one-dimensional (1D) surface brightness profile fitting (see Section 5 of Gao et al. 2019). In Figure 4 we illustrate this effect by comparing our B/T values with those of FD08 at fixed Hubble type. FD08 find systematically larger B/T than we do in disks of early to intermediate type, while their values are generally consistent with ours for Hubble types later than Sb. The difference is most dramatic in early-type disks.[6] The trend holds true for both classical and pseudo bulges.

We speculate that the systematic discrepancies between our results and those of FD08 are a direct consequence of the different fitting techniques applied to perform the bulge decomposition and the different input models used. We believe that our 2D fits provide more robust bulge parameters because our multicomponent models properly separate the bulge from

surrounding and overlapping substructures such as bars and lenses. The 1D approach of FD08 explicitly masks such substructures during the fitting. As shown by Gao & Ho (2017), this introduces large uncertainties in bulge parameters, especially in early-type disks where such substructures are most prevalent. We find better agreement with G09's results, presumably because his 2D decomposition technique is similar to ours, as are his criteria for classifying bulges. Nevertheless, the average bulge strength found by Gadotti ($\langle B/T \rangle = 0.33$ for classical bulges; $\langle B/T \rangle = 0.15$ for pseudo bulges) is also larger than ours (Figure 3). Although Gadotti's 2D method is certainly more trustworthy than 1D methods and does systematically treat bars, our 2D method (GALFIT; Peng et al. 2002, 2010) can handle a vastly more intricate array of internal substructures (Gao & Ho 2017; Gao et al. 2018, 2019), which ultimately leads to more robust bulge parameters. The statement of Kormendy (2016) that almost all pseudo bulges have $B/T \lesssim 0.35$ and $B/T \gtrsim 0.5$ guarantees that the bulge is classical still applies to our measurements, but it is not representative because $B/T \lesssim 0.2$ already includes most pseudo bulges, and only few bulges of either type have $B/T \gtrsim 0.5$. We echo previous works (e.g., Neumann et al. 2017) that stress that B/T is not a good parameter to distinguish between classical and pseudo bulges. The two bulge types simply overlap too heavily in B/T. The implication of such overlap at low B/T is discussed in Section 4.3.1.

Although classical bulges are not necessarily prominent, they do mostly have high surface brightnesses (Figure 2(e)), which is a direct outcome of their classification based on the Kormendy relation. It is noteworthy that the distribution of $\langle \mu_e \rangle$ shows the strongest separation between classical and pseudo bulges among all the structural parameters of bulges. A demarcation line at $\sim$18.5 mag arcsec^{-2} can isolate most of the classical bulges from the pseudo bulges. If any single bulge structural parameter were to be used to classify classical and pseudo bulges, $\langle \mu_e \rangle$ would be the best choice to produce consistent classifications based on the Kormendy relation. Adopting a boundary of $\langle \mu_e \rangle = 18.5$ mag arcsec^{-2} (in the R band) would correctly classify 87% of the pseudo bulges and 77% of the classical bulges.

S0 galaxies exhibit a wide range of bulge prominence, from traditionally bulge-dominated systems to those with bulges as weak as those in spirals of type Sc and later (Gao et al. 2018). However, in stark contrast to late-type spirals, which host mostly pseudo bulges, the bulges of S0s essentially all form a uniform sequence with the ellipticals on the Kormendy relation. In other words, almost all bulges in CGS S0s are classical. Based on this observation, Gao et al. (2018) argue that unless historically popular processes such as ram-pressure stripping can modify bulge structures substantially, most S0s cannot simply be descendants of faded late-type spirals (later than Sc). The present study further reinforces the conclusions of Gao et al. (2018). S0 bulges, independent of their B/T, almost exclusively occupy the upper envelope of the $\langle \mu_e \rangle - r_e$ plane. The weakest bulges found in S0s ($B/T \lesssim 0.1$) have surface brightnesses at least 2 mag brighter than the majority of the comparably weak bulges in late-type spirals (Figure 2(a)).

3.3. Bimodality or Continuity in Sérsic Indices

Figure 5 shows the distribution of CGS bulges on the Kormendy relation, with symbols color-coded according to their

---

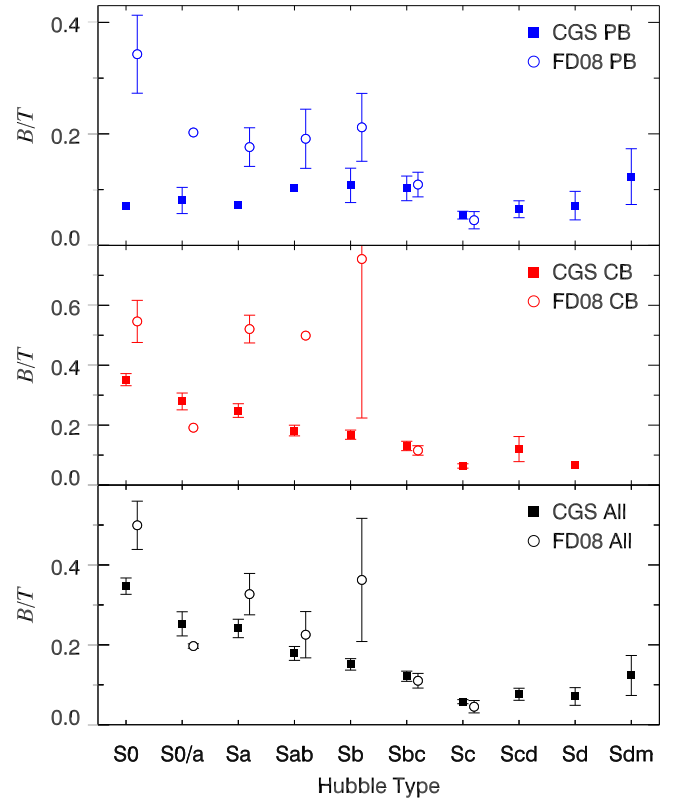[6] The S0/a bin is an exception probably because it contains only two galaxies.
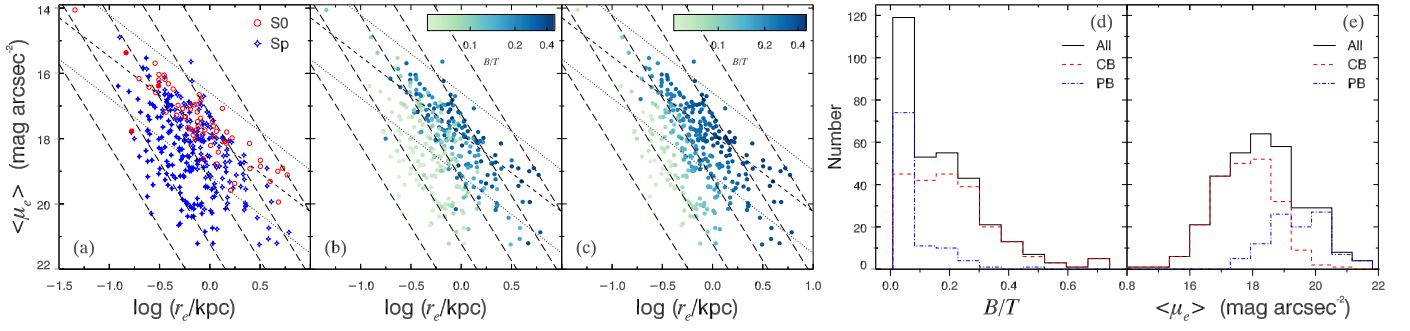
Figure 2. Bulges in the Kormendy relation: (a) distinguished by Hubble types, (b) color-coded according to their B/T, and (c) LOESS-smoothed version of panel (b). The filled symbols in panel (a) represent weak bulges ($B/T < 0.1$) in S0s (red) and spirals (blue). The best-fit relation and its 3σ boundary of the ellipticals are indicated by the short-dashed lines and dotted lines, respectively. The long-dashed lines approximately represent trajectories of constant bulge luminosities (ignoring cosmological effects). Panel (d) displays the distribution of B/T for the classical (red) and pseudo (blue) bulges; the overlap is significant. The two bulge types are better distinguished in surface brightness (e).
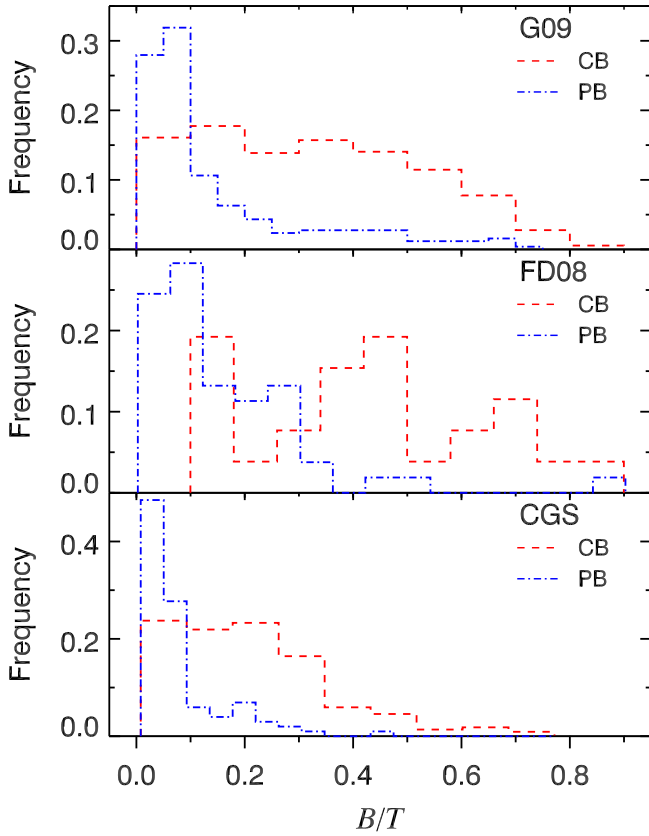

Figure 3. Distributions of B/T for classical (red) and pseudo (blue) bulges in (top) G09, (middle) FD08, and (bottom) CGS.

Figure 4. Distributions of B/T as a function of Hubble type in this study (CGS) with those from FD08 for (top) pseudo bulges, (middle) classical bulges, and (bottom) both bulge types combined. Symbols and error bars represent the mean and the error of the mean in each bin. Symbols are horizontally offset for clarity.

Sérsic indices. We show both the original data (panel (a)) and the LOESS-smoothed version (panel (b)) to facilitate visualization of the general trend. Along the direction of the Kormendy relation, bulges in general form a sequence of increasing Sérsic indices, from small to large r_e. This indicates that both classical and pseudo bulge can have small and large Sérsic indices, even if on average classical bulges have larger values. As with G09, we find that a minority of the pseudo bulges have Sérsic indices larger than 2. Meanwhile, a substantial fraction of classical bulges have $n < 2$ (panel (c)). Although on average pseudo bulges have smaller Sérsic indices than classical bulges, we do not observe the bimodal distribution of Sérsic indices reported in FD08, which was the

empirical basis of their Sérsic n-based classification criterion. FD08 identified pseudo bulges mainly based on their nuclear morphologies (presence of nuclear bars, rings, and spirals). However, the recent analysis of a small sample of double-barred galaxies by de Lorenzo-Cáceres et al. (2019) showed that most of the underlying bulges are classical. Moreover, Tabor et al. (2017) found some pressure-supported bulges in S0s with $n \approx 1$. In the same vein, Méndez-Abreu et al. (2018) discussed the lack of clear correspondence between bulge Sérsic index and their kinematics. Costantin et al. (2018) tested various observational diagnostics to separate classical and pseudo bulges and also concluded that Sérsic index is disfavored. Although Sérsic indices do carry physically
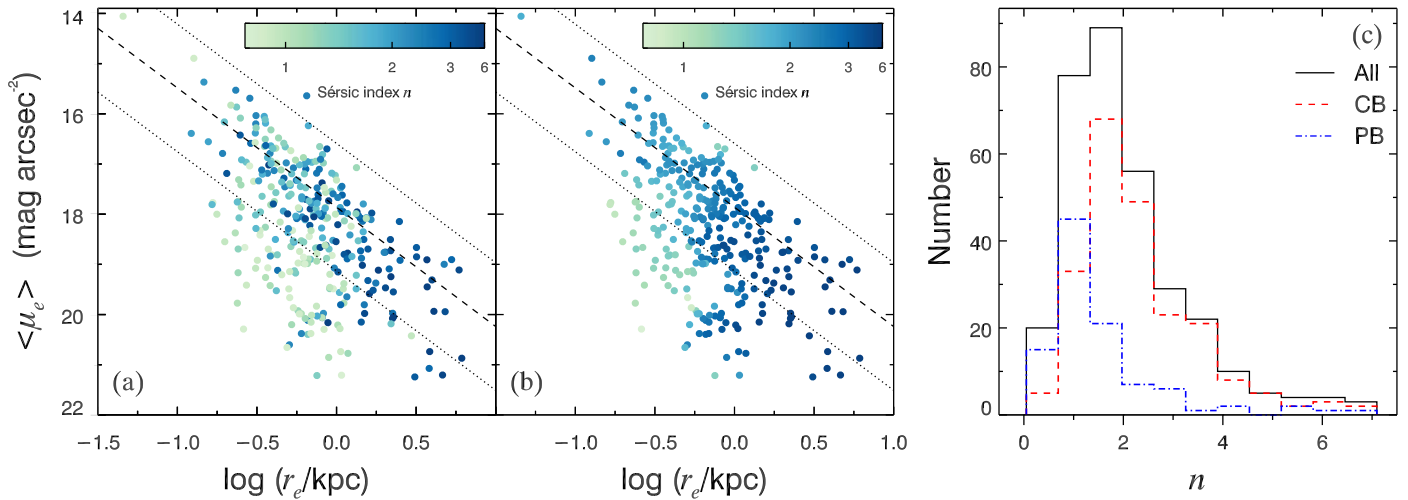
Figure 5. (a) Bulges in the Kormendy relation color-coded according to their Sérsic indices. Panel (b) is the same as panel (a), but the data have been LOESS-smoothed. The best-fit relation and its 3σ boundary of the ellipticals are indicated by short-dashed lines and dotted lines, respectively. Panel (c) shows the distribution of Sérsic indices for the classical (red) and pseudo (blue) bulges. The overlap is significant, and the bimodality presented in FD08 is not observed here.

significant information (e.g., mergers result in higher Sérsic indices: Aguerri et al. 2001; Eliche-Moral et al. 2006; Brooks & Christensen 2016), their large measurement error (Gadotti 2008) and sensitivity to spatial resolution (Balcells et al. 2003) and nuclear fine structures (Gao & Ho 2017) may hamper their application in classifying bulges. Combined with the discrepant classification results mentioned above, we suggest that $n = 2$ is not an appropriate demarcation line for separating classical and pseudo bulges. As with Neumann et al. (2017), we find that $n = 1.5$ is a better criterion; based on the statistics of CGS, this revised criterion would correctly classify 65% of the pseudo bulges and 74% of the classical bulges. Note that even with this modified threshold, Sérsic n is still a less effective classifier of bulge type than $\langle \mu_e \rangle$ (Section 3.2).

We also compare the distribution of bulge Sérsic n from CGS with those from FD08 and G09 (Figure 6). It is evident that both our measurements and those of G09 show significant overlap in n for classical and pseudo bulges, while in FD08 the two bulge types are well separated at $n \approx 2$. In contrast to the comparison of B/T at fixed Hubble type (Figure 4), Figure 7 shows that FD08's measurements show no noticeable systematic difference in bulge Sérsic n at fixed Hubble type for all bulges. This is also true for pseudo bulges. However, our values of n are systematically larger than those in FD08 for classical bulges in galaxies of all Hubble types.

### 3.4. Classical and Pseudo Bulges Share Similar Relative Bulge Size

Our decomposition demonstrates that classical and pseudo bulges have similar relative bulge size ($2r_e/D_{25}$), contrary to the results of FD08, who found that classical bulges have significantly larger relative sizes than pseudo bulges (Figure 8). We use D_{25} from Ho et al. (2011) for CGS galaxies and retrieve D_{25} of the sample in FD08 from HyperLeda[7] (Paturel et al. 2003). To investigate the origin of the discrepant results, we plot $2r_e/D_{25}$ as a function of Hubble type and B/T in Figure 9. We find that at fixed Hubble type or B/T, bulges in CGS and FD08 have similar mean relative bulge size, which increases as B/T increases; except for early-type disks (S0

---

[7] http://leda.univ-lyon1.fr/
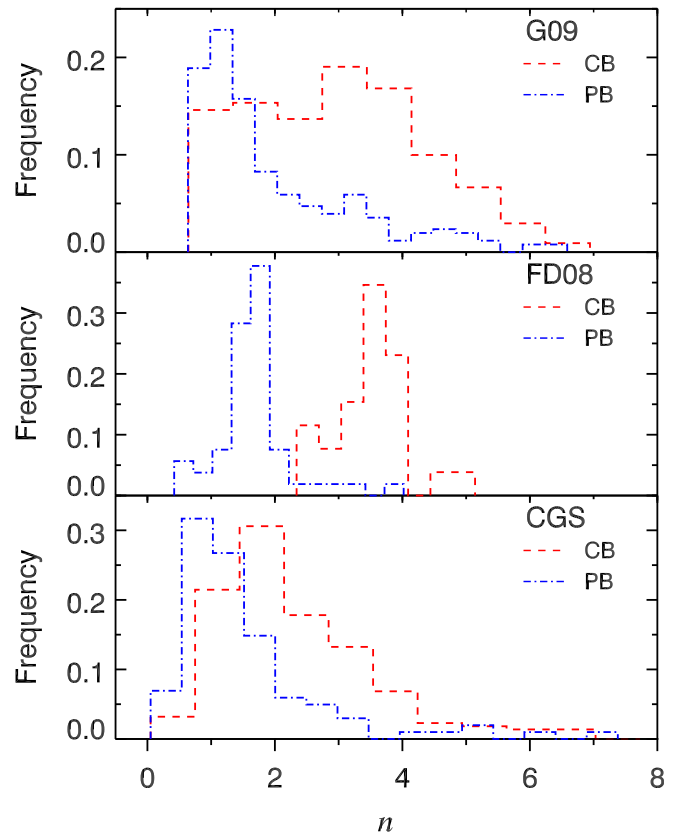
Figure 6. Distributions of Sérsic n for classical (red) and pseudo (blue) bulges in (top) G09, (middle) FD08, and (bottom) CGS.

and Sa), FD08's measurements are systematically larger than ours. It is also noteworthy that in the case of CGS, at a fixed B/T, pseudo bulges are more diffuse (larger $2r_e/D_{25}$) than classical bulges. It is evident in Figure 3 that the separation of B/T of classical and pseudo bulges in CGS is much less significant than in FD08. Therefore we speculate that the discrepant bulge relative size distributions of classical and pseudo bulges between CGS and FD08 is mainly due to the discrepant B/T measurements for the two bulge populations.
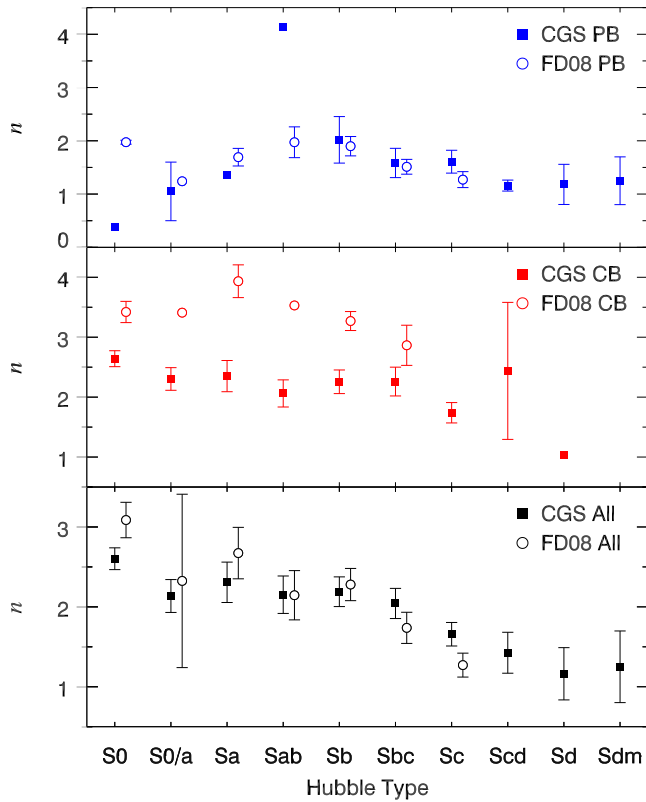
Figure 7. Distributions of bulge Sérsic n as a function of Hubble type in this study (CGS) with those from FD08 for (top) pseudo bulges, (middle) classical bulges, and (bottom) both bulge types combined. Symbols and error bars represent the mean and error of the mean in each bin. Symbols are horizontally offset for clarity.

Figure 8. Distributions of relative size of classical (red) and pseudo (blue) bulges in (top) FD08 and (bottom) CGS. The bulge effective radius r_e is normalized to the D_{25} isophotal diameter of the galaxy.

3.5. Bulge Dichotomy in Their Intrinsic Shapes

Intrinsic shapes of bulges have been extensively investigated by Méndez-Abreu et al. (2008, 2010), Costantin et al. (2017, 2018), and de Lorenzo-Cáceres et al. (2019). Without constraints from stellar kinematics, however, it is extremely difficult to measure the intrinsic shapes of individual bulges. Instead of looking into the intrinsic shapes, we turn to examining the statistics of their intrinsic flattenings. Figure 10 presents the apparent ellipticity (ϵ) distributions of classical and pseudo bulges. Classical bulges are on average apparently rounder than pseudo bulges. The two distributions are statistically different. A Kolmogorov–Smirnov test rejects the null hypothesis that the two samples are drawn from the same population at a probability of $P_{\mathrm{null}} \approx 10^{-4}$. The distribution of the apparent ellipticities of classical bulges is skewed markedly toward low ellipticities, while pseudo bulges have a broader distribution, reminiscent of the difference between apparent ellipticities of disks and spheroids (Sandage et al. 1970). Overlaying the apparent ellipticity distributions of CGS ellipticals and disk galaxies from Ho et al. (2011) reveals that classical bulges have similar apparent ellipticities with ellipticals, while the apparent ellipticities of pseudo bulges closely resemble those of disk galaxies. This is formally confirmed from Kolmogorov–Smirnov tests of the four populations: $P_{\mathrm{null}} = 0.51$ for classical bulges versus ellipticals, and $P_{\mathrm{null}} = 0.27$ for pseudo bulges versus disk galaxies. Classical bulges are intrinsically as round as ellipticals, and pseudo bulges are intrinsically as flattened as disks. This is consistent with the picture that classical bulges were formed in a manner similar to that of ellipticals, while pseudo
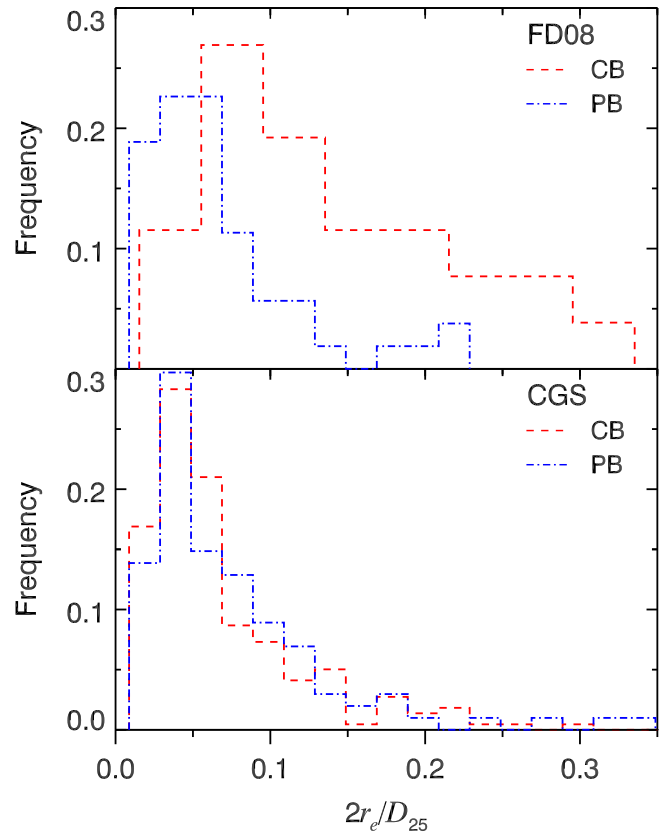
bulges originate from the gradual accumulation of disk material, having preserved enough memory of their disky origin to be recognized. However, as the apparent ellipticities of the two populations overlap with each other due to projection effects, we do not suggest using ellipticity as a criterion to separate classical and pseudo bulges.

### 3.6. Dichotomies in Classical and Pseudo Bulge Hosts

Section 3.5 shows that pseudo bulges are basically miniature disks. As disks are vulnerable to violent processes such as mergers, pseudo bulges are most likely to be found in late-type spirals, whose evolutionary history has been driven more by secular evolution than major mergers. Figure 11 examines the dependence of pseudo bulge incidence on Hubble type, stellar mass $M_\star$, and $B - V$ color. As expected, pseudo bulges are more frequent in galaxies with later Hubble types, lower stellar masses, and bluer optical colors. We also contrast the pseudo bulge incidence in barred and unbarred galaxies, but find no systematic differences between the two subsamples. This is counterintuitive because bars are often thought to be the main driver of secular evolution. We elaborate on this point in the next section.

In broad agreement with the literature, we also find that pseudo bulges prefer to reside in late-type spirals. Spirals with Hubble types later than Sbc are indeed the most active manufacturing sites of pseudo bulges. At least $\sim$60% of them host pseudo bulges. However, our pseudo bulge incidence in most Hubble types is significantly smaller than previously found.
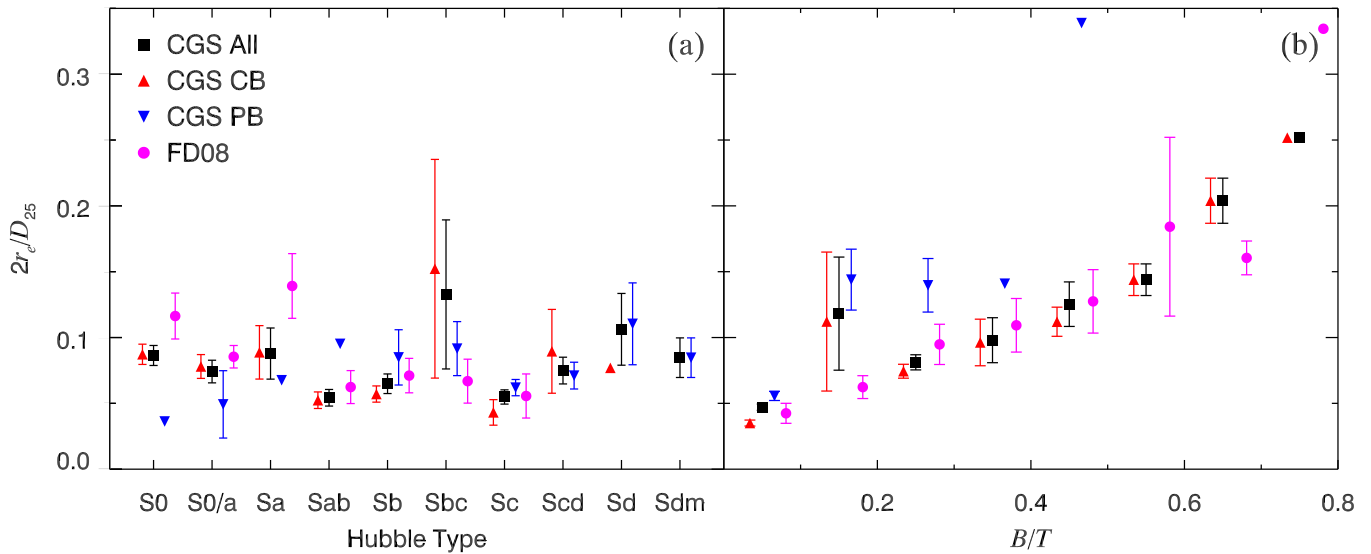
Figure 9. Relative size of the bulge as a function of (a) Hubble type and (b) B/T for all CGS bulges (black), CGS classical bulges (red), CGS pseudo bulges (blue), and bulges in FD08 (magenta). The bulge effective radius r_e is normalized to the D_{25} isophotal diameter of the galaxy. Symbols and error bars represent mean and error of the mean in each bin, respectively. Symbols are horizontally offset for clarity.
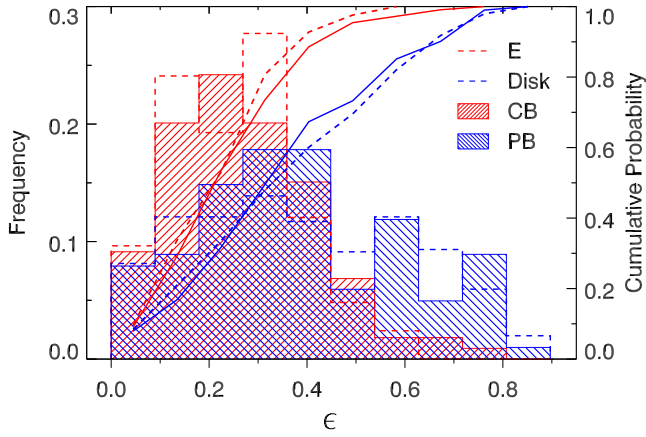
Figure 10. Distributions of apparent ellipticities of classical (red) and pseudo (blue) bulges, CGS ellipticals (red dashed), and CGS disks galaxies (blue dashed). The cumulative probability of each subgroup is overlaid with the same line style.

Kormendy & Kennicutt (2004) summarized the statistics of pseudo bulges as a function of Hubble type from the literature. Based on morphologies and Sérsic indices of 75 galaxies with *Hubble Space Telescope (HST)* images analyzed by Carollo et al. (1997), they found that 69%, 50%, 22%, 11%, and 0% of S0–Sa, Sab, Sb, Sbc, and Sc and later type galaxies host classical bulges, respectively. The general trend of increasing incidence of pseudo bulges toward late Hubble types is consistent with our measurements. However, their pseudo bulge fraction is higher than ours (Table 1). The same holds true for the work of Kormendy & Kennicutt (2004), who, reanalyzing the sample of Carollo et al. (2002) based on *HST V*- and *H*-band images, concluded that 50%, 40%, 56%, 94%, and 100% of S0+Sa, Sab, Sb, Sbc, and Sc–Sm galaxies host exponential bulges. Exponential bulges are considered a close proxy for pseudo bulges. Taken at face value, their pseudo bulge fraction is again systematically higher than ours. We do not know the exact reason of the quantitative discrepancy because differences in bulge-to-disk decomposition techniques, wavelength effects,

spatial resolution of the data, sample size (CGS is significantly larger than the above-cited samples), and, more directly, the classification criteria affect the outcome.

3.7. Pseudo Bulges and Their Relation to Bars

In Section 3.6 we already noted that barred galaxies do not host more pseudo bulges than unbarred galaxies at fixed Hubble type, stellar mass, or optical color. This is unexpected if bars drive secular evolution, as is often surmised (e.g., Kormendy & Kennicutt 2004; Wang et al. 2012; Lin et al. 2017; Chown et al. 2019). Figure 12 investigates this issue in the context of the Kormendy relation. Again, we find no indication that the presence of a bar has any effect on skewing objects below the Kormendy relation of the ellipticals (i.e., toward the locus of pseudo bulges). This seems to be in conflict with the notion that bars help drive gas inflow and to build pseudo bulges. However, one should bear in mind that bars can also contribute to bulge growth through dissipationless processes, most notably via the buckling instability. The difference in formation physics between bar buckling instability and bar-driven gas inflow motivated Athanassoula (2005) to advocate that boxy/peanut bulges should be regarded as a separate class from other pseudo bulges. The bulge-like structure produced by bar buckling instability is not necessarily weak (small B/T) or disky (small n). This is illustrated in Figure 12, where the bulges of buckled barred galaxies occupy the locus of classical bulges with large n ($\gtrsim 2$) and B/T ($\gtrsim 0.2$). The classifications of the buckled bars come from Li et al. (2017), who visually identified boxy/peanut bulges and barlenses, both of which are regarded as the same phenomena viewed from different inclination angles, based on variations of isophotal shapes in the bar region. We conclude that the Kormendy relation mostly only selects pseudo bulges that are formed from dissipative secular processes. We do not know whether this is because of the inherent limitations of the Kormendy relation—given its substantial intrinsic scatter—or because bulges with buckled bar features are not genuine pseudo bulges. We observed a similar phenomenon before (Gao et al. 2018). The bulges of some S0 galaxies bear the
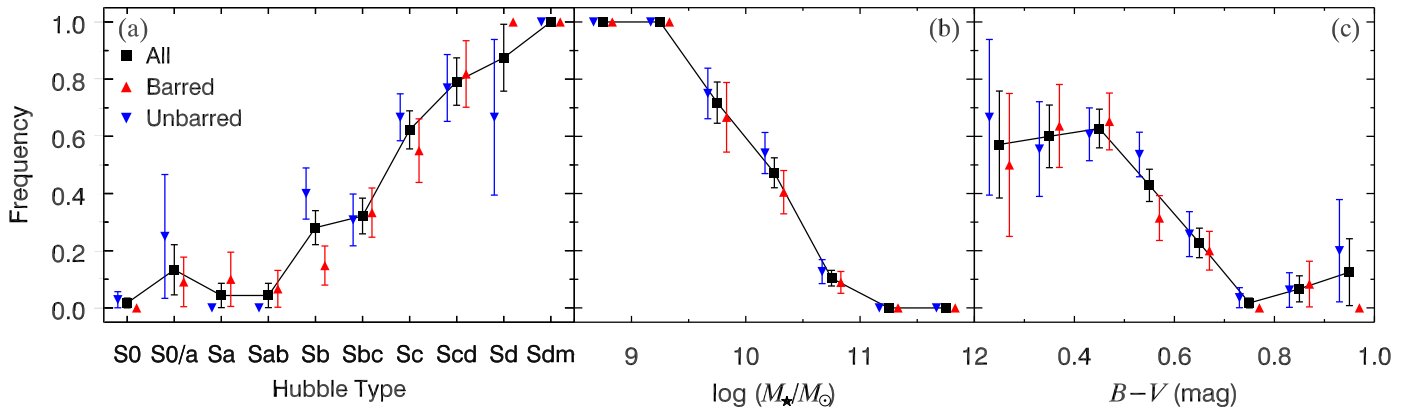
Figure 11. Frequency of pseudo bulges as a function of the (a) Hubble type, (b) stellar mass, and (c) optical color of the host galaxy. Black symbols with connected lines represent all galaxies, and red and blue symbols are barred and unbarred galaxies, respectively. Error bars are calculated assuming a binomial distribution. Symbols are horizontally offset for clarity.

appearance of pseudo bulges, but are not recognized as such on the Kormendy relation. Disky features do not reliably signify the overall photometric structure or the star formation activities of the bulge. Given that buckled bars occur most frequently in early-type disks, where mergers were once operative, they may not dominate the overall bulge structure.

Bars play a critical role in facilitating gas inflow, the raw material for star formation in galaxy centers and hence for pseudo bulge growth. It is instructive to control for the amount of available gas and then compare pseudo bulge properties of barred and unbarred galaxies. While we expect the pseudo bulge fraction to increase toward more gas-rich galaxies, a natural consequence of the increase of specific gas content toward galaxies with higher specific star formation rate and later Hubble type (Roberts & Haynes 1994, and references therein), more available gas does not seem to be related to increased pseudo bulge fraction for barred galaxies (Figure 13). At fixed gas fraction, the pseudo bulge fraction of barred galaxies is not significantly different than that of unbarred galaxies. If there is any systematic trend at all, it goes in the opposite direction. Bulge prominence (B/T) and normalized bulge size ($2r_e/D_{25}$) of pseudo bulges do not show any systematic trends with gas content, while Sérsic n seems to increase toward gas-poor galaxies, but the results are inconclusive because of the small number statistics in the three most gas-poor bins. Again, at fixed gas fraction, the presence of a bar has no relation to B/T, Sérsic n, or $2r_e/D_{25}$. Because of the small number statistics, we cannot afford to further control for galaxy stellar mass, but comparison of the stellar mass distribution of barred and unbarred galaxies rules out stellar mass as an important factor. If barred galaxies were to host more and stronger pseudo bulges, then, to account for the similar pseudo bulge properties of barred and unbarred galaxies we would expect the stellar masses of barred galaxies to deviate systematically from those of unbarred galaxies. Comparison of the stellar masses of barred and unbarred galaxies at fixed gas fraction does not reveal any systematic differences.

To summarize: pseudo bulges identified by the Kormendy relation rarely include bulges with boxy/peanut features (or barlenses when viewed face-on). Therefore, the pseudo bulges identified in this paper largely refer to those formed out of material accumulated from central gas inflows, not from the bar buckling instability. We find no evidence that at a fixed gas

fraction bars help the formation or growth of pseudo bulges. Implications of these results are addressed in Section 4.3.2.

4. Discussion

4.1. Bulge Definition: Comparison with Previous Studies

Measurements of bulge parameter depend on which part of the galaxy is regarded as the bulge. As illustrated in Gao & Ho (2017) and Gao et al. (2018, 2019), we consistently adopt the convention that bulges refer to extra light above the inner extrapolation of disks or bars, after excluding any possible nuclei. Note that disks here do not necessarily refer to a single exponential component, but instead to the analytic function or combination of functions that best describes the disk surface brightness. Therefore, the bulge component includes the contribution from nuclear bars or rings and boxy/peanut bulges (thickened part of bar), if present. We do not model these substructures as individual, separate components in addition to the bulge, although some are actually part of the bar (e.g., boxy/peanut bulges). If we model all distinct disky features in the bulge region as individual components, we risk isolating every pseudo component from the rest of the photometric bulge. This betrays our goal of characterizing bulge dichotomies in the local Universe. We acknowledge that other studies with different scientific goals may adopt different bulge definitions from ours, and therefore their bulge parameters may not be comparable to ours. For example, Läsker et al. (2016) isolated everything else to extract the pure classical bulges to study black hole–bulge relations. The study of de Lorenzo-Cáceres et al. (2019) modeled nuclear bars separately because the latter were the objects of interest. In the same vein, we adopt the definition that best suits our specific goal, which is to characterize the structural properties of the overall photometric bulge, regardless of how many subcomponents it might have. Our definition is similar to that of G09, only that our disk models are more detailed than his, causing the bulge parameters to be different (Figure 3).

FD08 employed a different method than we did to measure bulge parameters. Because of the limitations of their 1D technique, nonaxisymmetric components (e.g., bars and lenses) cannot be modeled simultaneously with the bulge and disk, and FD08 excluded them from the fit. Their bulge definition also differs subtly from ours because they masked nuclear rings or bars

Table 1
Percentage of Pseudo Bulge Hosts in Bins of Hubble Type and Stellar Mass

Hubble Type	S0	S0/a	Sa	Sab	Sb	Sbc	Sc	Scd	Sd	Sdm
All	2 ± 2	13 ± 9	4 ± 4	4 ± 4	28 ± 6	32 ± 6	62 ± 7	79 ± 8	88 ± 12	100 ± 0
Barred	0 ± 0	9 ± 9	10 ± 10	7 ± 6	15 ± 7	33 ± 9	55 ± 11	82 ± 12	100 ± 0	100 ± 0
Unbarred	3 ± 3	25 ± 22	0 ± 0	0 ± 0	40 ± 9	31 ± 9	67 ± 8	77 ± 12	67 ± 27	100 ± 0

$\log M_\star / M_\odot$	8.5–9.5	9.5–10.0	10.0–10.5	10.5–11.0	11.0–12.0
All	100 ± 0	72 ± 7	47 ± 5	10 ± 3	0 ± 0
Barred	100 ± 0	67 ± 12	41 ± 8	9 ± 4	0 ± 0
Unbarred	100 ± 0	75 ± 9	54 ± 7	13 ± 4	0 ± 0
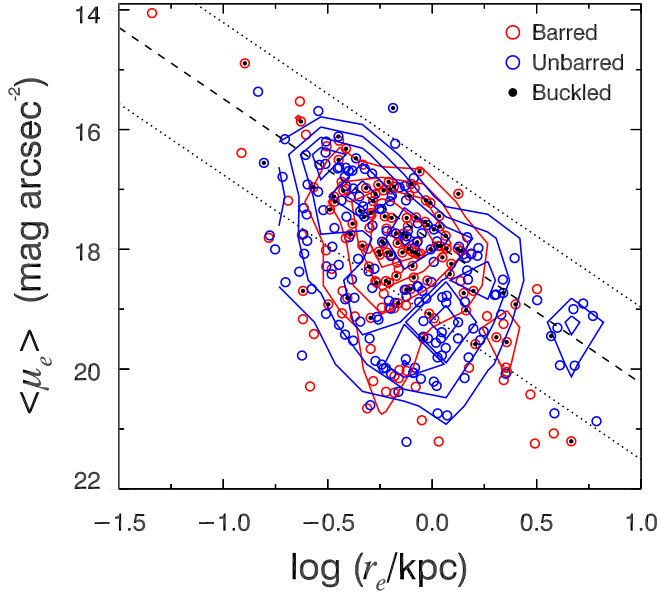
Figure 12. Bulges on the Kormendy relation for barred (red) and unbarred (blue) galaxies. The buckled bars recognized by Li et al. (2017) are marked by solid black dots; due to different strategy of identifying barred galaxies, some of the buckled bars are designated unbarred according to the classification of this paper. The best-fit relation and its 3σ boundary of the ellipticals are indicated by short-dashed lines and dotted lines, respectively. The barred and unbarred galaxies do not show any preference to host classical or pseudo bulges. Most of the boxy/peanut bulges follow the Kormendy relation of the ellipticals.
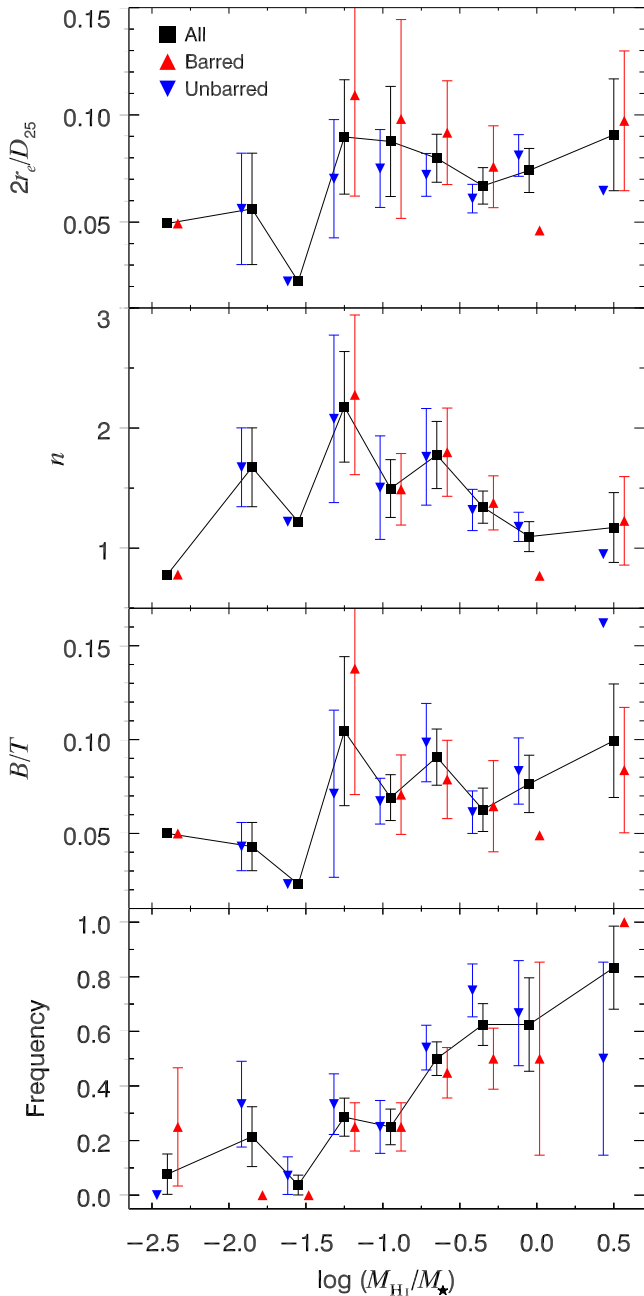
from their fits. This might affect bulge structural parameters, but should not alter B/T much (Gao & Ho 2017; de Lorenzo-Cáceres et al. 2019). To better understand the underlying reasons for the discrepancy between our results and those of FD08, we closely examined the 14 galaxies in common between the two samples. Fortunately, none of the galaxies contains complications from nuclear disky features, affording a relatively straightforward comparison between FD08's technique and ours.

Figure 14 illustrates the bulge-dominated region for the overlapping objects. Because FD08 did not provide the position angles of their bulges, we assume that their values are the same as ours. We find that except for NGC 1022 and NGC 3521, where FD08's bulges are treated as nuclei in our fits, both studies ascribe the same physical entity to the bulge. The discrepancies in the resulting bulge parameters mostly reflect differences in data quality, in the techniques applied, and in details of the model construction. Our 2D approach generally allows for more direct and robust model construction to account for the multicomponent nature of nearby disk galaxies.

Figure 15 compares the bulge parameters from this study with those from FD08 for the comparison sample. Taking into consideration the large uncertainties of the parameters in FD08, their measurements, apart from a few outliers, are broadly consistent with ours, and there are no significant systematic trends. Unfortunately, the small size of the comparison sample prevents us from drawing any firm conclusions as to the origin of the systematic discrepancies in B/T and relative bulge size of early-type disks. Among the 14 galaxies in common, there are only two Sa galaxies, one Sa/0 galaxy, and no S0s, where the differences in B/T and relative bulge size are most significant. As mentioned above, various reasons could be responsible for the differences. Our smaller B/T in early-type disks, where classical bulges are most abundant, in conjunction with our classification criterion that includes less prominent classical bulges (small n), results in a less clear separation between classical and pseudo bulges in the B/T distribution when compared with FD08 (Figure 3). This leads to both bulge types having similar relative sizes (Figure 8), as argued in Section 3.4. We did not find substantial systematic differences in bulge Sérsic n for the full sample at fixed Hubble type (Figure 7) or for the subset of galaxies in common between CGS and FD08 (Figure 15(b)). Therefore, the significantly different distributions of n (Figure 6) are probably due to the different classification criteria used by us and FD08.

We also note that the consistency of the classifications is poor. Only 4 of the 14 bulges have consistent classifications. If we adopted $n = 2$ to separate classical and pseudo bulges in CGS, our classifications would agree much better with those of FD08 (10/14). This suggests that adopting different classification criteria is the major source of the inconsistency. In contrast to our study that relies on scaling relations, FD08 used nuclear morphologies to distinguish bulge types. While such an approach is physically meaningful and has the merit of being immune from potential bias in bulge structural parameters, it is not quantitative, relying on subjective, visual morphological classification. Moreover, it may not work well in composite bulges whose disky features are not fundamental to the overall bulge nature (e.g., Erwin et al. 2015; Gao et al. 2018).

On the other hand, Kormendy (2013, 2016) and Fisher & Drory (2016) warned against using the Kormendy relation to identify pseudo bulges because high-density pseudo bulges would risk being misclassified. Given that scaling relations have been demonstrated to be useful in distinguishing objects of different nature, an immediate question is why pseudo bulges should follow the scaling relation of ellipticals. A plausible explanation is that these are composite bulges, which contain contributions from secular evolution and therefore can

various bulge-type indicators and found that using the Kormendy relation alone can recover classifications based on multiple criteria to a high success rate. Without access to other measurements that are useful to classify bulge types (e.g., stellar kinematics and stellar populations), we are unable to follow such a strategy. We add to their advocacy, however, by showing that pseudo bulges selected by the Kormendy relation exhibit properties that consistently imply a disky origin and that the Sérsic index is not an appropriate indicator of bulge types.

Using the classifications from FD08 for the comparison sample, we find that 30% of the pseudo bulges have $n > 2$ in CGS, and 25% of the classical bulges have $n < 2$ in CGS; in FD08, all the pseudo bulges have $n < 2$, and all the classical bulges have $n > 2$. This suggests that differences in Sérsic n measurements tend to weaken the separation of n of classical and pseudo bulges in CGS. The next section demonstrates that the weakening of the bimodality is not due to the relative large number of classical bulges in the CGS sample.
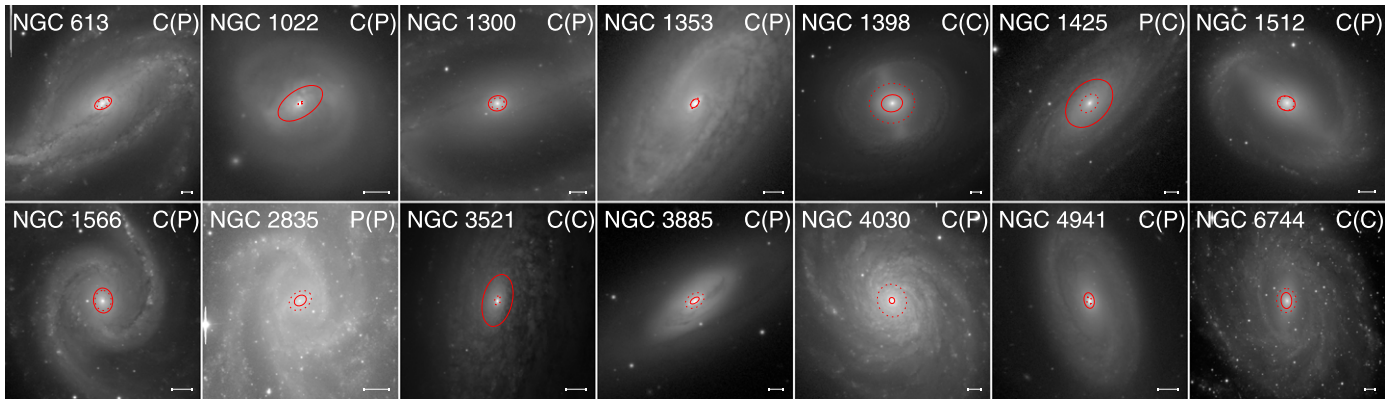
To summarize: the small number of overlapping galaxies prevents us from investigating the cause of the discrepancies between our study and that of FD08. We speculate that differences in data quality, fitting techniques, model construction, and classification criteria all play a role.

4.2. Conflicts with Previous Results

Some of our population statistics differ from those of previous studies (Sections 3.2–3.4, and 3.6). First, the basis of the widely adopted criterion for bulge classification—the bimodal distribution of Sérsic indices—cannot be reproduced in our measurements. Does the discrepancy stem merely from the different methods used to classify bulge type? After all, FD08 identified pseudo bulges based on their nuclear morphologies in *HST* images, while we define pseudo bulges as low surface brightness outliers in the Kormendy relation.

We do not think that this can be the whole story. If we suppose that classical and pseudo bulges have distinct distributions in Sérsic index and can be well separated at $n \approx 2$, we would have 125 classical bulges and 195 pseudo bulges in CGS, similar to but slightly different from the relative numbers in FD08 (26 versus 53). In contrast, the G09 sample is dominated by $n \geqslant 2$ bulges (421 versus 267). The different relative number of classical to pseudo bulges could erase the bimodality in the global distribution of bulge Sérsic index. We explore the effects of varying the relative fraction of classical to pseudo bulges on the global distribution of bulge Sérsic index in the FD08 sample by matching the statistics of CGS and G09. Following the style presented in Figure 9 of FD08, we plot the distribution of log n in Figure 16. Although we observe a gentle dip at log $n \approx 0.3$ for CGS (unfilled black histogram), it is still not comparable with the significant deficit of bulges in the FD08 sample at log $n \approx 0.4$ (filled black histogram) after matching the relative number of classical to pseudo bulges. The same holds for the comparison of the G09 sample (unfilled red histogram) with the FD08 sample (filled red histogram). There is always a strong dip at log $n \approx 0.4$ for the FD08 sample, regardless of whether it is dominated by classical or pseudo bulges. In concert with the comparisons for the objects in common (Figure 15) and at fixed Hubble type (Figure 7), we suspect that the small sample size and selection effects of the FD08 sample may be responsible for their deficit of bulges with $n \approx 2$–3.

Figure 13. Correlation of pseudo bulge properties with the gas fraction of their hosts. From top to bottom, the panels show normalized pseudo bulge sizes, Sérsic indices, bulge-to-total ratios, and detection frequency as a function of H I gas fraction for all galaxies (black), barred galaxies (red), and unbarred galaxies (blue). There are no systematic differences between barred and unbarred galaxies. Errors of pseudo bulge frequency are calculated assuming a binomial distribution. Symbols and error bars in the other panels represent mean and error of the mean in each gas fraction bin, respectively. Symbols are horizontally offset for clarity.

be recognized using Sérsic index or nuclear morphology. Unfortunately, this issue cannot be resolved in the context of a binary classification scheme, namely classifying bulges as either classical or pseudo bulges. In such an exercise, without independent measurements of the relative importance of violent to secular processes in bulge growth, it is difficult to tell which criterion is superior. However, it is possible to assess the robustness of such classifications. For example, as mentioned in Section 1, Neumann et al. (2017) have done so by comparing

Figure 14. *R*-band images of 14 CGS galaxies in common with the FD08 sample. The bulge region is overlaid with a red ellipse (solid = CGS; dashed = FD08), whose semimajor axis represents the bulge effective radius, with axis ratio and orientation following the best-fit model. Bulge types are indicated in the upper right corner of each image (C = classical; P = pseudo); the classication from FD08 is given in parentheses. The scale bar in the lower right corner represents 1 kpc.

Instead, among all the bulge structural parameters considered in CGS, the clearest separation between classical and pseudo bulges is seen in $\langle \mu_e \rangle$. This, of course, is a natural outcome of using the Kormendy relation to classify bulges. A clean separation in $\langle \mu_e \rangle$ is ensured because pseudo bulges happen to have a similar range of r_e as classical bulges. Thus, $\langle \mu_e \rangle$ is an effective single criterion for classifying bulge types consistent with classifications based on the Kormendy relation.

Second, we reiterate that 1D fitting systematically overestimates bulge luminosities (see also Section 5 of Gao et al. 2019). Early 1D studies often adopted a de Vaucouleurs (1948) law ($n = 4$) for the bulge component, which was later shown to overestimate the bulge contribution (e.g., Kent 1985; Kodaira et al. 1986; Simien & de Vaucouleurs 1986). FD08 presented significantly improved 1D fitting results by adopting better model assumptions and carefully masking morphological features that deviate from their simplified model. Still, comparison of our results with those from FD08 shows that this effect, most severe in early-type disk galaxies, together with the different classification criteria applied, leads to significant differences between their B/T distributions and ours, both for classical and pseudo bulges. The same holds for bulge sizes. Whereas we find that classical and pseudo bulges have similar relative sizes, FD08 concluded that the former have larger relative sizes than the latter (Section 3.4). 1D fitting comes with several ambiguities and inherent weaknesses that cannot be overcome (see Section 1 of Gao & Ho 2017 for an overview). The most serious limitation of the 1D technique is that it does not use the full 2D spatial information in the image and therefore does not account for the full range of complexity intrinsic to most galaxy disks. Substructures such as bars and lenses cannot be adequately modeled in 1D fitting and therefore cannot be isolated properly from the bulge, often causing the bulge to be overestimated (e.g., Kent 1985; Kodaira et al. 1986; Simien & de Vaucouleurs 1986). Although FD08 strove to mask these features in their fits, Gao & Ho (2017) showed that such a compromised strategy amplifies uncertainties in the resulting bulge parameters due to further loss of information. Our results agree better with those of G09, whose methodology, like ours, can account for bars. Indeed, we employ the latest version of GALFIT to treat a variety of other substructures as well (Gao & Ho 2017). Therefore we conclude that our measurements, based on better technique and more realistic models, are more accurate than published 1D fitting results, and the differences mostly reflect improvement of measurements.

Finally, we derive a lower pseudo bulge fraction in early-type disks than in studies that use nuclear morphologies and/or Sérsic indices to classify bulges (Figure 11; Section 3.6). This mismatch is probably largely related to differences in classification criteria. We have already noted inconsistencies between classifications based on nuclear morphologies with those based on the Kormendy relation (Figure 3 of Gao et al. 2018). S0 bulges bearing disky features such as nuclear bars and rings cannot be distinguished from classical bulges in terms of their location on the Kormendy relation. We attributed this apparent inconsistency to the fact that the bulges bearing disky features in early-type disks are most likely composite bulges, the bulk of whose mass was assembled early and fast, and secular processes subsequently superposed disky features on top of a preexisting classical bulge. The disky features also help to lower the Sérsic index of the bulge (see the case of NGC 1326 in Section 4.7 of Gao & Ho 2017). In our estimation, bulge classifications based on the Kormendy relation are more secure than those that rely on nuclear morphology, which neither comprehensively nor reliably signifies the overall photometric structure and formation history of the bulge (see also Fisher et al. 2009).

### 4.3. Implications for Bulge Formation and Evolution

4.3.1. Violent versus Secular Processes

We summarize the key results from this study that are useful for diagnosing the nature of bulges:

1. Most pseudo bulges have $B/T \lesssim 0.1$ and low surface brightness ($\langle \mu_{e,R} \rangle \gtrsim 18.5$ mag arcsec^{-2}), while classical bulges have a broad distribution of B/T and exhibit higher surface brightness ($\langle \mu_{e,R} \rangle < 18.5$ mag arcsec^{-2}).
2. Pseudo bulges have low Sérsic indices ($n \lesssim 2$), while classical bulges have a broad distribution of n.
3. Classical bulges have an ellipticity distribution consistent with that of elliptical galaxies, while pseudo bulges have a broad distribution of ellipticity that is reminiscent of disks.
4. Pseudo bulges preferentially reside in late-type spirals that are less massive and more gas rich.

These properties consistently support the prevailing hypothesis that pseudo bulges are disky components masquerading as
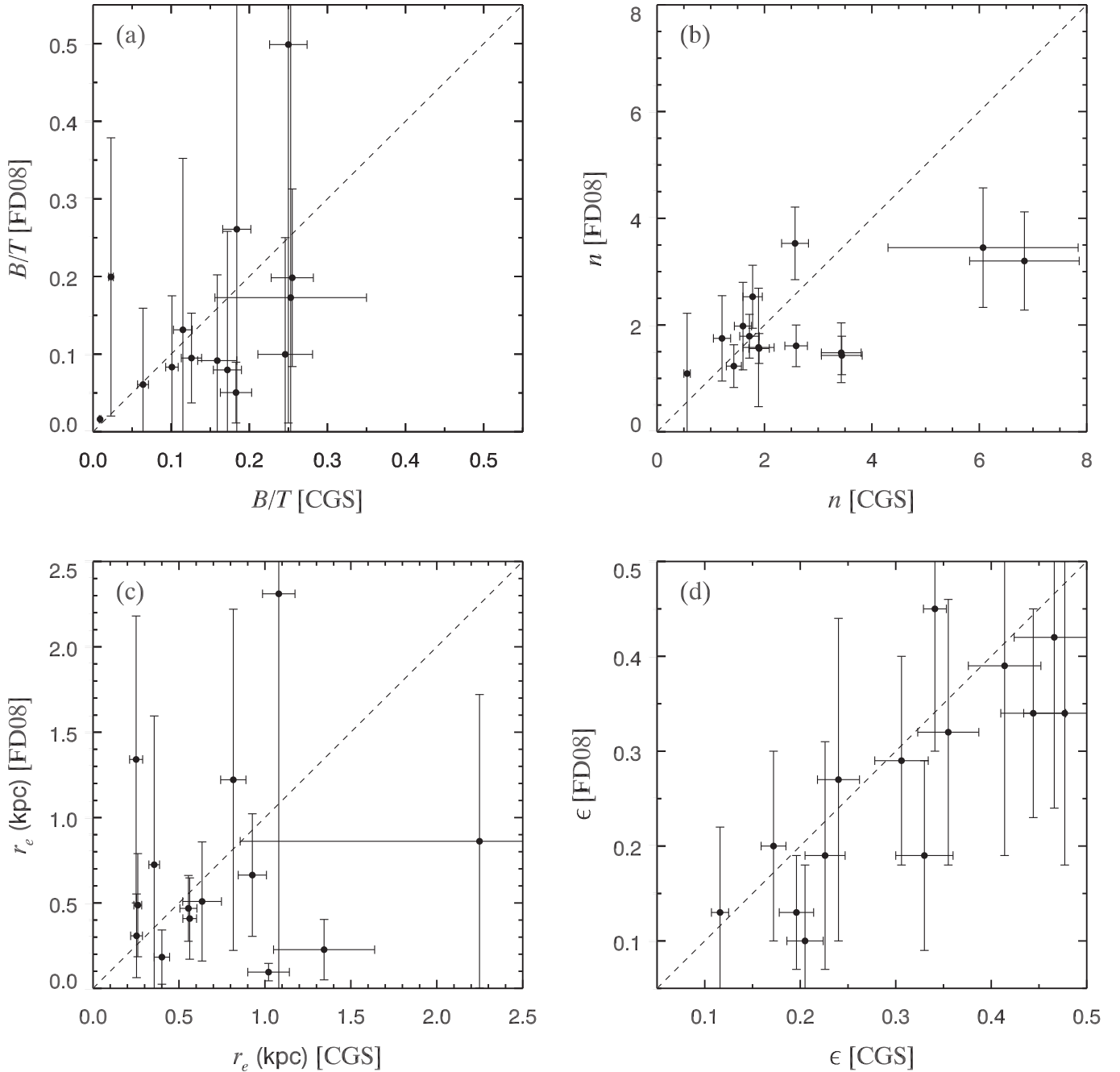
Figure 15. Comparison of CGS (*R* band) bulge parameters with those obtained by FD08 (*V* band) for the 14 galaxies in common between the two studies, for (a) B/T, (b) n, (c) r_e, and (d) ϵ. Dashed lines are one-to-one relations.

bulges. Pseudo bulges were formed from stars born out of gas accumulated in the central regions of the galaxy (Kormendy & Kennicutt 2004; Sellwood 2014; Tonini et al. 2016; Izquierdo-Villalba et al. 2019). Because their formation resembles the assembly of galaxy disks, pseudo bulges manifest themselves as diffuse (low $\langle \mu_e \rangle$), approximately exponential ($n \approx 1$), and intrinsically flattened (broad distribution of ϵ) structures. Secular processes being inefficient and gradual, only relatively modest masses accumulate in the center (small B/T). The products of secular processes are most frequently found in late-type spirals because these systems have more fuel to

feed central star formation and generally have experienced a more placid merger history. However, it is unclear which mechanisms are mainly responsible for driving gas inflow. Nonaxisymmetries such as bars, lenses or ovals, and spiral arms contribute to secular evolution, among them bars that are often thought to be the most effective. Intriguingly, the analysis in Section 3.7 shows no preference for barred galaxies to host pseudo bulges. We revisit this issue in Section 4.3.2.

On the other hand, the broad distribution of B/T and n of classical bulges implies a variable formation efficiency. Ellipticals and classical bulges can be made viably through
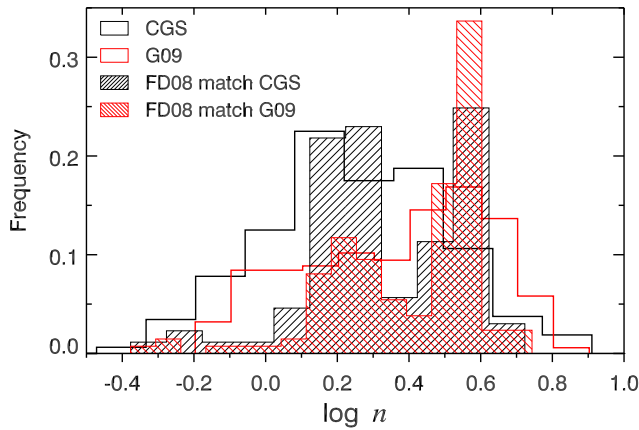
Figure 16. Comparison of bulge Sérsic index distributions for the sample of CGS (unfilled black histogram), G09 (unfilled red histogram), and FD08 (filled black and red histogram) after matching the relative number of classical to pseudo bulges. Bulges with $\log n < -0.5$ in CGS are omitted.

major mergers (Hopkins et al. 2009a, 2009b, 2010; Brooks & Christensen 2016; Tonini et al. 2016; Rodriguez-Gomez et al. 2017). Violent relaxation of preexisting stars and central starbursts resulting from the rapid inflow of gas create bulges of high Sérsic indices and pressure-supported stellar orbits. The efficiency of bulge formation depends on the gas fraction of the merger, and the degree to which the merger remnant reacquires a stellar disk (Hopkins et al. 2009a, 2009b, 2010). Minor mergers can also contribute to the formation or growth of classical bulges, albeit in a less prominent (Aguerri et al. 2001; Eliche-Moral et al. 2006; Hopkins et al. 2010) and more complicated manner. Minor mergers can either contribute directly to the bulge or trigger disk instabilities and indirectly contribute to bulge growth in a secular manner. The density of the satellite is a determining factor: a dense satellite more likely survives to the center and contributes to the growth of a classical bulge, while a diffuse satellite can be tidally disrupted halfway (Aguerri et al. 2001; Eliche-Moral et al. 2006). More massive satellites, of course, lead to more dramatic effects.

Moreover, coalescence of giant clumps in high-redshift disks can form classical bulges (Noguchi 1999; Bournaud et al. 2007, 2009; Elmegreen et al. 2008; Bournaud 2016). The disks of gas-rich, vigorously star-forming, high-redshift galaxies fragment into massive clumps of stars and gas and exhibit irregular morphologies as a result of stellar feedback and gravitational instability. The clumps in what are commonly referred to as clumpy or chain galaxies then migrate inward through dynamical friction and merge into a bulge. Although the physical processes are driven by disk instability, they are nothing like the secular evolution in $z \approx 0$ disks because the migration and coalescence of clumps operate on much shorter timescales (several hundreds of Myr; see Noguchi 1999 and Genzel et al. 2008). Clump coalescence, along with violent relaxation, creates highly concentrated, dispersion-supported, high-[α/Fe] ratio spheroids that resemble ellipticals, which, by definition, are classical bulges (Immeli et al. 2004; Elmegreen et al. 2008). The accretion timescale, mass, and mass density of the galaxies can produce a broad spectrum of bulge prominence, down to values as small as $B/T \approx 0.1$ (Noguchi 1999; Bournaud et al. 2007). This seems to be consistent with

the observed broad distribution of B/T for classical bulges (Figure 3). However, not all investigators agree that bulges originate from clumps. Oklopčić et al. (2017) use cosmological hydrodynamic simulations with a realistic stellar feedback treatment to show that clumps are short-lived and do not systematically migrate inward.

The broad outlines for the formation of classical and pseudo bulges seem more or less in order. The secular processes that build pseudo bulges at $z \approx 0$ are inefficient and produce mostly weak bulges. The resulting disky component retains enough memory of its origin that it can be distinguished from classical bulges in various respects. Classical bulges form with variable efficiency through rapid processes involving violent relaxation and gaseous dissipation at an early epoch. Their structural parameters follow the scaling relations (e.g., Kormendy relation and FP) of ellipticals, and they are spheroids instead of flattened structures like pseudo bulges. The formation picture, however, still has some loose ends. Some studies maintain that mergers can make pseudo bulges (Wang et al. 2015; Eliche-Moral et al. 2018; Sauvaget et al. 2018), although the pseudo bulges may still be the products of secular processes of the rebuilt disks after the gas-rich mergers settle down. Inoue & Saitoh (2012) suggest that clump coalescence can lead to pseudo bulges, even if, overall, the ultimate fate of clumps is still controversial (Oklopčić et al. 2017). A quantitative comparison between our measurements with theoretical predictions would be highly desirable, but this lies beyond the scope of this paper. Previous studies have revealed possible inconsistencies. According to Weinzirl et al. (2009), semianalytic ΛCDM models predict too many prominent bulges compared with observations. At the same time, other authors consider the pseudo bulges to be overabundant compared to cosmological predictions (Kormendy & Fisher 2008; Kormendy et al. 2010). It is also puzzling to see no signs of a classical bulge in massive disk galaxies such as NGC 4565 (Kormendy & Barentine 2010). The lower pseudo bulge fractions in early-type disks reported in this study perhaps helps alleviate the tension.

4.3.2. The Driving Engines of Secular Evolution

In Section 3.7 we found that bars do not bear any obvious relation to pseudo bulges, not even in gas-rich galaxies. This is counterintuitive because bars, the strongest nonaxisymmetric structure in the disk, are thought to drive efficient gas inflow. Perhaps it indicates that nonaxisymmetries other than bars, such as lenses or ovals and spiral arms, also participate in driving gas inflow. As these additional nonaxisymmetries are ubiquitous features in disk galaxies, the presence or absence of pseudo bulges does not have to rely on bars alone.

Still, because other nonaxisymmetries are weaker than bars, we need to understand why barred galaxies have pseudo bulges of comparable strength and frequency as unbarred galaxies (Figure 13). We caution that the observed B/T of pseudo bulges represents the accumulated growth of their prolonged history, and is not necessarily related to the present-day observable properties of the galaxy, such as its current gas fraction and presence of a bar. Today's gas-poor galaxies may once have been gas rich. At any rate, pseudo bulges are generically weak ($B/T \lesssim 0.1$), and hence the host does not need to be extraordinarily gas rich to provide the fuel. This may explain why the B/T of pseudo bulges does not depend on

current gas fraction (Figure 13). Another outstanding issue pertains to whether bars are long-lived (Athanassoula et al. 2013) or not (Bournaud & Combes 2002). Central mass concentrations such as black holes and compact bulges weaken and even dissolve bars (Combes 1996; Shen & Sellwood 2004; Bournaud et al. 2005), but they can be regenerated from gas accretion (Combes 1996; Block et al. 2002; Bournaud & Combes 2002; Bournaud et al. 2005). Therefore, present-day unbarred galaxies may once have been barred, during which time their pseudo bulges were built. If so, we expect that at fixed B/T and gas fraction, the pseudo bulges of barred galaxies should have younger stellar populations. This hypothesis should be tested in the future. The evolutionary state of the bar may also matter. In gas-rich systems where bars have the best chance to make a difference between barred and unbarred galaxies, bars may have developed later and are weaker when mature (Athanassoula et al. 2013). Mature bars suffer from buckling instability and form boxy/peanut bulges, which reduce gas inflow to the very center (Fragkoudi et al. 2016). Bar-driven secular evolution itself may be self-regulated: the very growth of a pseudo bulge may weaken the bar and thereby curtail its own growth rate. This may weaken any systematic differences between barred and unbarred systems. Finally, external perturbations, such as ram-pressure striping, flybys, and minor mergers, may also promote gas inflows (e.g., Moore et al. 1996, 1998, 1999; Bekki 1999; Bekki & Couch 2011; Kaviraj 2014; Poggianti et al. 2017). Such external effects would be incredibly difficult to disentangle from internal secular processes in our sample.

To summarize: despite the lack of clear observational evidence that bars directly relate to the pseudo bulge phenomenon, the above considerations prevent us from drawing any firm conclusions about their actual role.

5. Summary

We use robustly measured structural parameters of a large, homogeneous sample of 320 lenticular and spiral galaxies to investigate the Kormendy ($\langle\mu_e\rangle$ versus r_e) relation of their bulge components. The bulge parameters are derived from detailed 2D decomposition of high-quality R-band images drawn from CGS. We critically discuss the empirical classification of bulge types, reexamine the statistical properties of classical and pseudo bulges, and consider their physical implications.

Our principal results are as follows.

1. Despite the ambiguities in classification of bulge types, we find that pseudo bulges selected as low-$\langle\mu_e\rangle$ outliers of the Kormendy relation established by elliptical galaxies generally show physical properties consistent with their presumed disky origin.
2. The distribution of bulge Sérsic indices is not bimodal. We recommend abandoning the common practice of adopting $n \approx 2$ to distinguish between classical and pseudo bulges.
3. In line with Gadotti (2009) and Neumann et al. (2017), we recommend using the Kormendy relation as a promising alternative to using the Sérsic index to classify bulges.

4. Pseudo bulges have low Sérsic indices, most having $n \lesssim 2$, with the distribution peaking at $n \approx 1$, consistent with disk-like profiles. Most pseudo bulges are weak, comprising only $B/T \lesssim 0.1$ of the total light.
5. Classical bulges display a broad distribution in B/T and n and are on average more prominent than pseudo bulges, despite their significant overlap in B/T.
6. Pseudo bulges are intrinsically more flattened structures compared with classical bulges. The ellipticities of pseudo bulges are consistent with those of disks.
7. Pseudo bulges reside most frequently in less massive, gas-rich, late-type spirals.
8. Contrary to naive expectations, barred galaxies do not host more pseudo bulges or more prominent pseudo bulges than unbarred galaxies.

The statistical properties of our sample reveal a number of quantitative differences compared to previous studies that can be understood in terms of our improved method of 2D image decomposition and different classification criteria applied. In qualitative agreement with previous studies, we suggest that pseudo bulges formed through internal secular processes in the large-scale disk, where nonaxisymmetries drive gas inflow and build up central overdensities through star formation. Their disky origin is still encoded in their low surface brightnesses, near-exponential radial profiles, and flattened geometry. Classical bulges formed via violent processes similar to those in elliptical galaxies.

Appendix
R-band Structural Parameters of CGS Ellipticals

The CGS ellipticals provide the fiducial scaling relations for comparison with bulges. We performed single-Sérsic fits to derive their global structural parameters (n, μ_e, and r_e) in the R band. Although Li et al. (2011) give access to nonparametric measurements of the structural parameters, we consider our parametric analysis necessary because we wish to avoid possible systematic biases due to measurement technique. Comparison of the two sets of measurements (Figure 17, top panels) reveals that that Sérsic fits indeed yield values of μ_e and r_e that are systematically larger than the nonparametric ones. This is expected because Sérsic fits integrate the flux to infinity, whereas nonparametric methods measure the flux only within the radius where the galaxy light fades into the noise. The tests of Trujillo et al. (2001) show that the differences between the two kinds of measurements depend on the Sérsic index and the size of the galaxy relative to the aperture applied to measure its flux: the larger the galaxy size and Sérsic index, the more significant the differences between the parametric and nonparametric measurements because more light would be missed by the nonparametric methods. The bottom panels of
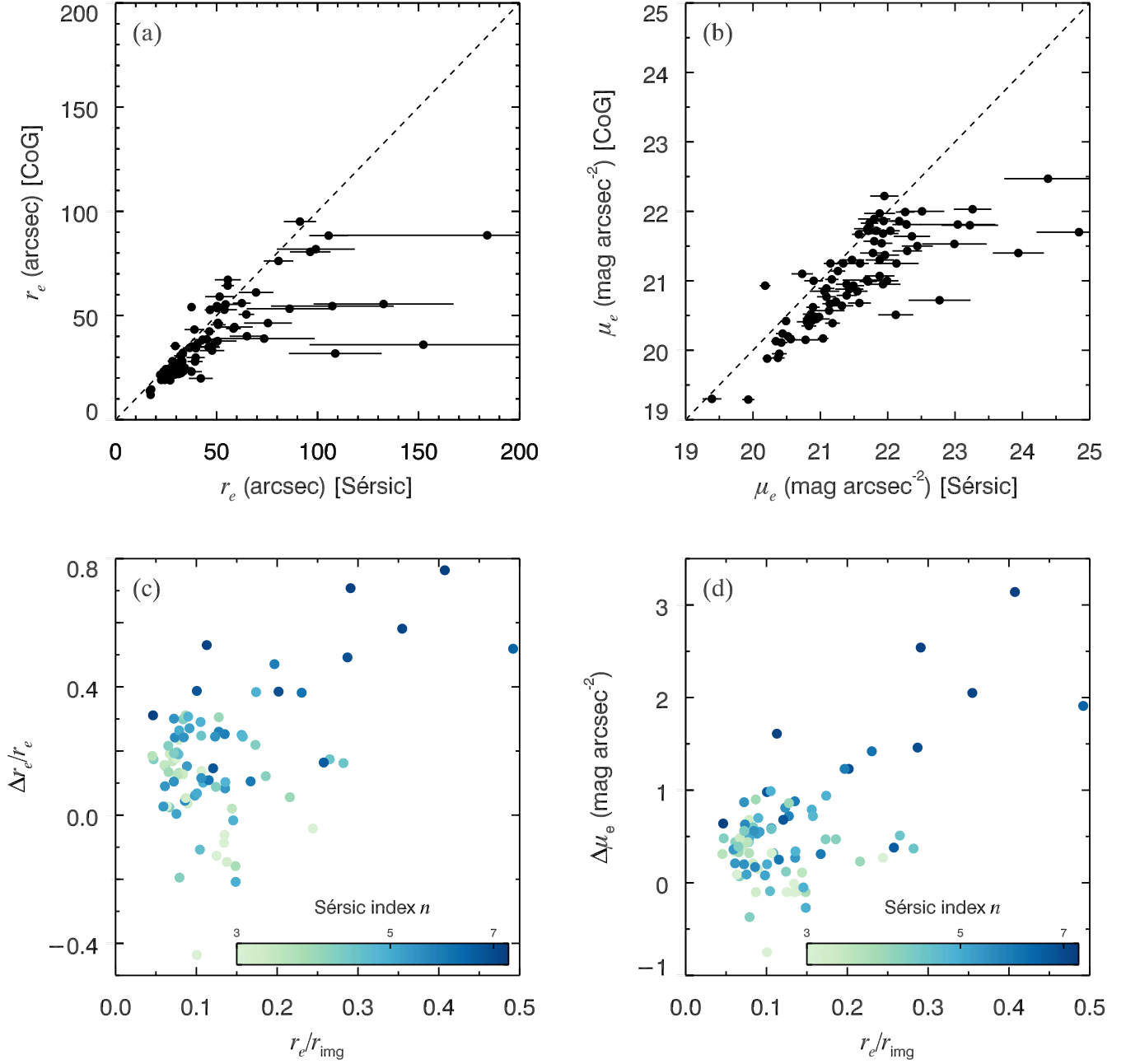
Figure 17. Comparison of Sérsic structural parameters (a) r_e and (b) μ_e with nonparametric ones based on the curve-of-growth (CoG) analysis of the CGS ellipticals. Dependence of the differences in (c) r_e and (d) μ_e on galaxy size normalized by the image size and on Sérsic index.

Figure 17 confirm this trend. Galaxies with larger normalized r_e and larger n show larger offsets in the two structural parameters.

Although we choose Sérsic-based parameters for the ellipticals to facilitate a consistent comparison with the bulges, there are concerns about these measurements that need to be addressed. First, the measurements are model dependent because we already know that ellipticals can be better fit by multiple Sérsic components (Huang et al. 2013a). Second, we do not know the light distributions beyond the limiting surface brightness of the images, so it is dangerous to recklessly extrapolate to infinity. The three-component Sérsic fits of Huang et al. (2013a), which conform to the two-phase scenario for the origin of ellipticals (Huang et al. 2013b), in principle should describe the outermost component of the galaxy more accurately and therefore provide more reasonable extrapolation at large radii. Huang et al. (2016) presented three-component Sérsic fits of a subset of the CGS ellipticals in the R band. Figure 18 shows good agreement between the total magnitudes derived from our single-Sérsic fits and their three-Sérsic fits.
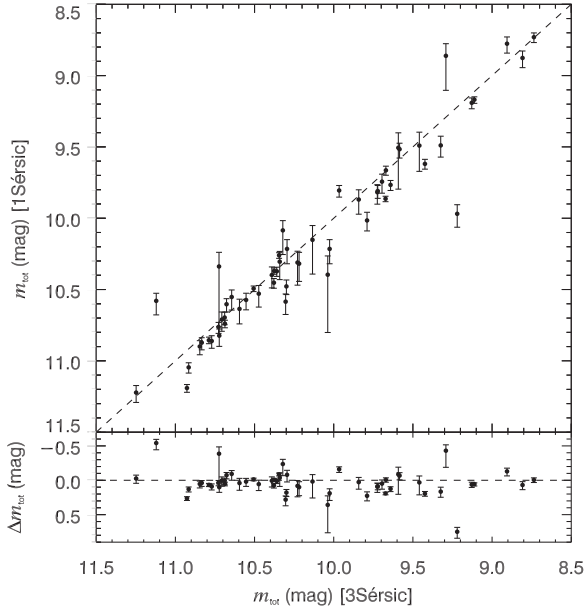
Figure 18. Comparison of total magnitudes of the CGS ellipticals obtained through single-Sérsic fits with those through three-Sérsic fits. There is no significant systematic bias ($\langle \Delta m_{tot} \rangle = 0.03 \pm 0.19$ mag).

Systematic bias is negligible (0.03 mag), and the rms scatter is 0.19 mag. This comparison makes us confident that the total light of the ellipticals obtained from single-Sérsic fits is reasonable, at least when compared with state-of-art parametric measurements.

We only have to deal with the extreme outliers. There are four galaxies (NGC 1172, 2865, 4936, and 4976) that exhibit offsets larger than twice the rms. We remeasure their μ_e, $\langle \mu_e \rangle$, and r_e using the curve-of-growth method, but using total magnitudes obtained from the three-Sérsic fits as input instead of the total magnitudes obtained from the nonparametric method. However, this method failed in the case of NGC 4936 because its r_e lies beyond the image boundary, so we apply no further corrections for it. We also correct for NGC 1439 because it appears as an outlier in the Kormendy relation. Correcting the structural parameters of these four galaxies has little effect on the scaling relation.

The best-fit models for the ellipticals are displayed in Figure 19, and their structural parameters are listed in Table 2.

Table 2
Best-fit Parameters of the CGS Ellipticals

Name	$\langle \mu_e \rangle$ (mag arcsec^{-2})	n	r_e (kpc)	ϵ
(1)	(2)	(3)	(4)	(5)
ESO 185–G054	20.76 ± 0.20	4.94 ± 0.26	18.71 ± 2.46	0.269 ± 0.000
IC 1459	19.31 ± 0.09	5.19 ± 0.12	6.61 ± 0.34	0.261 ± 0.000
IC 1633	21.56 ± 0.25	6.69 ± 0.34	35.50 ± 5.58	0.167 ± 0.000
IC 2311	19.15 ± 0.19	5.18 ± 0.29	2.90 ± 0.34	0.043 ± 0.000
IC 2597	20.35 ± 0.12	4.97 ± 0.17	7.04 ± 0.54	0.284 ± 0.000
IC 3370	19.54 ± 0.08	3.92 ± 0.15	4.53 ± 0.23	0.164 ± 0.000
IC 3896	19.97 ± 0.29	5.49 ± 0.42	7.03 ± 1.31	0.208 ± 0.002
IC 4296	20.28 ± 0.19	4.97 ± 0.23	13.37 ± 1.56	0.084 ± 0.001
IC 4742	20.05 ± 0.29	3.89 ± 0.51	8.28 ± 1.71	0.192 ± 0.002
IC 4765	22.53 ± 0.59	6.05 ± 0.66	52.04 ± 21.53	0.362 ± 0.001
IC 4797	18.71 ± 0.09	4.52 ± 0.16	3.37 ± 0.20	0.399 ± 0.001
IC 4889	19.02 ± 0.06	4.07 ± 0.09	3.56 ± 0.13	0.336 ± 0.000
IC 5328	19.62 ± 0.12	4.26 ± 0.19	4.93 ± 0.36	0.288 ± 0.002
NGC 596	19.59 ± 0.06	5.14 ± 0.10	3.30 ± 0.12	0.126 ± 0.001
NGC 636	20.22 ± 0.23	6.42 ± 0.40	4.63 ± 0.63	0.119 ± 0.000
NGC 720	18.85 ± 0.07	3.22 ± 0.09	4.36 ± 0.20	0.420 ± 0.000
NGC 1052	18.88 ± 0.06	3.97 ± 0.10	2.96 ± 0.10	0.295 ± 0.000
NGC 1172	21.05 ± 0.86	⋯	7.03 ± 3.41	0.207 ± 0.002
NGC 1199	19.79 ± 0.13	4.61 ± 0.20	4.84 ± 0.37	0.249 ± 0.001
NGC 1209	18.92 ± 0.05	4.58 ± 0.10	3.85 ± 0.13	0.524 ± 0.000
NGC 1339	18.87 ± 0.08	4.58 ± 0.16	1.78 ± 0.09	0.284 ± 0.000
NGC 1340	19.13 ± 0.07	3.59 ± 0.12	3.51 ± 0.17	0.354 ± 0.000
NGC 1374	19.48 ± 0.05	4.62 ± 0.09	2.66 ± 0.09	0.097 ± 0.000
NGC 1379	19.56 ± 0.05	3.12 ± 0.08	2.47 ± 0.08	0.019 ± 0.000
NGC 1395	19.65 ± 0.09	4.33 ± 0.12	5.89 ± 0.33	0.163 ± 0.001
NGC 1399	19.64 ± 0.10	4.58 ± 0.12	5.93 ± 0.35	0.093 ± 0.001
NGC 1404	18.06 ± 0.11	3.31 ± 0.18	2.14 ± 0.15	0.136 ± 0.001
NGC 1407	20.17 ± 0.14	4.42 ± 0.17	9.32 ± 0.85	0.046 ± 0.000
NGC 1426	19.87 ± 0.18	5.09 ± 0.33	3.72 ± 0.42	0.350 ± 0.000
NGC 1427	20.11 ± 0.11	5.45 ± 0.18	4.84 ± 0.35	0.299 ± 0.000
NGC 1439	21.02 ± 0.41	⋯	6.95 ± 1.58	0.090 ± 0.000
NGC 1453	20.07 ± 0.20	5.63 ± 0.29	10.81 ± 1.35	0.163 ± 0.001
NGC 1521	20.32 ± 0.18	5.25 ± 0.26	10.91 ± 1.22	0.300 ± 0.001
NGC 1549	19.64 ± 0.10	4.96 ± 0.14	4.64 ± 0.29	0.103 ± 0.000
NGC 1600	20.32 ± 0.20	3.75 ± 0.27	12.39 ± 1.72	0.329 ± 0.002

Table 2
(Continued)

Name	$\langle\mu_e\rangle$ (mag arcsec^{-2})	n	r_e (kpc)	ϵ
(1)	(2)	(3)	(4)	(5)
NGC 1700	19.11 ± 0.17	5.33 ± 0.28	5.31 ± 0.55	0.287 ± 0.000
NGC 2305	19.70 ± 0.14	4.82 ± 0.19	4.98 ± 0.43	0.251 ± 0.000
NGC 2325	20.18 ± 0.11	2.95 ± 0.12	5.53 ± 0.41	0.364 ± 0.000
NGC 2434	19.74 ± 0.18	4.71 ± 0.27	4.21 ± 0.48	0.089 ± 0.001
NGC 2663	20.05 ± 0.29	4.73 ± 0.35	13.22 ± 2.57	0.332 ± 0.001
NGC 2865	18.44 ± 0.17	...	2.28 ± 0.27	0.250 ± 0.000
NGC 2986	20.44 ± 0.11	5.57 ± 0.17	10.70 ± 0.76	0.151 ± 0.000
NGC 3078	19.23 ± 0.17	5.00 ± 0.27	4.93 ± 0.51	0.241 ± 0.000
NGC 3087	19.64 ± 0.16	5.33 ± 0.24	5.95 ± 0.59	0.149 ± 0.000
NGC 3091	20.24 ± 0.19	5.24 ± 0.27	10.81 ± 1.32	0.286 ± 0.001
NGC 3136	20.68 ± 0.43	6.73 ± 0.58	12.43 ± 3.52	0.264 ± 0.001
NGC 3250	19.26 ± 0.12	3.85 ± 0.17	6.30 ± 0.47	0.256 ± 0.001
NGC 3258	20.16 ± 0.20	4.80 ± 0.26	7.74 ± 0.97	0.127 ± 0.001
NGC 3268	21.22 ± 0.50	5.51 ± 0.61	14.45 ± 4.92	0.203 ± 0.000
NGC 3557	19.54 ± 0.10	4.58 ± 0.13	8.11 ± 0.49	0.242 ± 0.000
NGC 3585	19.98 ± 0.17	6.24 ± 0.25	8.22 ± 0.86	0.445 ± 0.001
NGC 3923	20.20 ± 0.14	4.71 ± 0.17	10.69 ± 0.97	0.343 ± 0.001
NGC 3962	19.96 ± 0.11	4.91 ± 0.16	7.49 ± 0.54	0.202 ± 0.000
NGC 4696	20.72 ± 0.12	2.99 ± 0.13	16.65 ± 1.46	0.219 ± 0.000
NGC 4709	21.32 ± 0.38	5.70 ± 0.47	15.42 ± 3.80	0.155 ± 0.000
NGC 4742	18.06 ± 0.08	7.99 ± 0.17	1.26 ± 0.06	0.400 ± 0.000
NGC 4760	20.73 ± 0.19	4.42 ± 0.25	12.68 ± 1.61	0.155 ± 0.001
NGC 4767	19.23 ± 0.10	4.17 ± 0.16	5.03 ± 0.33	0.423 ± 0.001
NGC 4786	19.37 ± 0.10	4.08 ± 0.16	6.87 ± 0.44	0.232 ± 0.000
NGC 4936	20.21 ± 0.17	4.14 ± 0.22	8.13 ± 0.94	0.170 ± 0.001
NGC 4976	19.02 ± 0.37	...	3.25 ± 0.82	0.320 ± 0.001
NGC 5011	20.17 ± 0.15	5.06 ± 0.22	7.23 ± 0.68	0.158 ± 0.000
NGC 5018	18.52 ± 0.06	4.39 ± 0.10	4.79 ± 0.18	0.297 ± 0.000
NGC 5044	20.27 ± 0.12	3.12 ± 0.14	8.23 ± 0.69	0.060 ± 0.000
NGC 5061	19.50 ± 0.15	6.48 ± 0.25	5.70 ± 0.53	0.099 ± 0.001
NGC 5077	19.14 ± 0.14	4.56 ± 0.21	5.45 ± 0.47	0.302 ± 0.001
NGC 5328	19.80 ± 0.14	5.23 ± 0.21	7.94 ± 0.66	0.313 ± 0.000
NGC 5419	20.63 ± 0.18	4.55 ± 0.23	15.78 ± 1.95	0.210 ± 0.000
NGC 5791	19.21 ± 0.09	3.98 ± 0.15	4.43 ± 0.26	0.425 ± 0.000
NGC 5796	19.55 ± 0.14	5.06 ± 0.22	5.23 ± 0.45	0.131 ± 0.000
NGC 5812	19.32 ± 0.10	5.24 ± 0.17	3.63 ± 0.23	0.044 ± 0.000
NGC 5898	19.27 ± 0.20	4.59 ± 0.28	3.88 ± 0.49	0.019 ± 0.001
NGC 5903	20.48 ± 0.24	4.87 ± 0.31	9.05 ± 1.39	0.232 ± 0.000
NGC 6851	18.89 ± 0.07	4.20 ± 0.14	2.74 ± 0.13	0.266 ± 0.000
NGC 6868	20.04 ± 0.18	4.94 ± 0.23	8.08 ± 0.90	0.186 ± 0.000
NGC 6876	20.19 ± 0.08	3.05 ± 0.10	9.05 ± 0.52	0.136 ± 0.000
NGC 6909	20.05 ± 0.14	4.37 ± 0.25	5.33 ± 0.49	0.442 ± 0.000
NGC 6958	19.18 ± 0.07	5.17 ± 0.11	3.55 ± 0.16	0.144 ± 0.000
NGC 7029	19.41 ± 0.07	5.23 ± 0.11	4.75 ± 0.19	0.364 ± 0.000
NGC 7145	20.42 ± 0.15	4.94 ± 0.21	4.41 ± 0.42	0.036 ± 0.000
NGC 7196	19.28 ± 0.13	4.58 ± 0.21	5.41 ± 0.42	0.217 ± 0.000
NGC 7507	18.80 ± 0.09	4.99 ± 0.13	4.11 ± 0.22	0.038 ± 0.000
NGC 7796	20.03 ± 0.13	4.91 ± 0.19	8.13 ± 0.66	0.153 ± 0.000

Note. Col. (1): galaxy name. Cols. (2)–(5): average effective surface brightness, Sérsic index, effective radius, and ellipticity. The parameters are measured in the R band and have been corrected for Galactic extinction.

(This table is available in machine-readable form.)
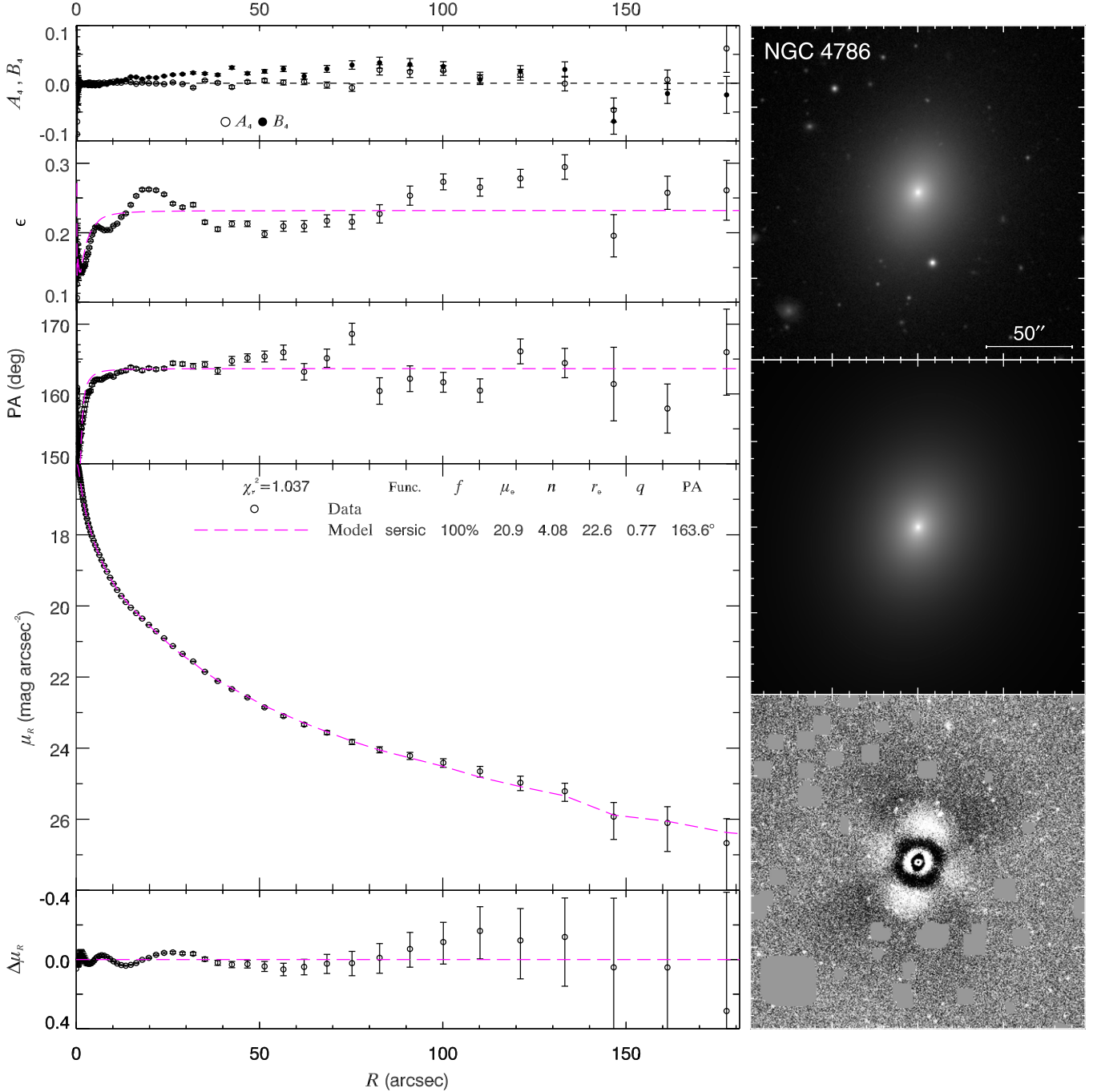
Figure 19. Best-fit model of NGC 4786. The left panels display the isophotal analysis of the 2D image fitting. From top to bottom the panels show the radial profiles of the fourth harmonic deviations from an ellipse (A_4 and B_4), ellipticity (ϵ), position angle (PA), R-band surface brightness (μ_R), and fitting residuals ($\triangle\mu_R$). Profiles of the data and model are encoded consistently with different symbols, line styles, and colors, as explained in the legends. The text to the right of the legends gives detailed information on each component; from left to right, the columns describe the radial profile functions (Sérsic), the light fractions, the effective surface brightness μ_e, the Sérsic index n, the effective radius r_e, the axis ratio q, and the PA. Note that the surface brightness profile of the model is generated by fixing the geometric parameters to those of the data surface brightness profile. The right panels display from top to bottom the grayscale R-band image, the best-fit model image, and the residual image. The images are shown using the same logarithmic stretch for the data and model image, and histogram equalization stretch for the residual image. All images are cropped to have the same size of $1.5D_{25}$, with D_{25} the isophotal galaxy diameter at $\mu_B = 25$ mag arcsec^{-2}, and are centered on the galaxy centroid, with north up and east to the left. The complete figure set for 83 elliptical galaxies is available in the online journal.)

(The complete figure set (83 images) is available.)

ORCID iDs

Hua Gao (高桦) ⓘ https://orcid.org/0000-0003-1015-5367
Luis C. Ho ⓘ https://orcid.org/0000-0001-6947-5846
Aaron J. Barth ⓘ https://orcid.org/0000-0002-3026-0562
Zhao-Yu Li ⓘ https://orcid.org/0000-0001-5017-7021

References

Aguerri, J. A. L., Balcells, M., & Peletier, R. F. 2001, A&A, 367, 428
Allen, P. D., Driver, S. P., Graham, A. W., et al. 2006, MNRAS, 371, 2
Athanassoula, E. 2005, MNRAS, 358, 1477
Athanassoula, E., Machado, R. E. G., & Rodionov, S. A. 2013, MNRAS, 429, 1949
Balcells, M., Graham, A. W., Domínguez-Palmero, L., & Peletier, R. F. 2003, ApJL, 582, L79
Bekki, K. 1999, ApJL, 510, L15
Bekki, K., & Couch, W. J. 2011, MNRAS, 415, 1783
Bender, R. 1987, MitAG, 70, 226
Bender, R. 1988, A&A, 193, L7
Bender, R., Burstein, D., & Faber, S. M. 1992, ApJ, 399, 462
Bertin, G., Ciotti, L., & Del Principe, M. 2002, A&A, 386, 149
Binggeli, B. 1994, in ESO/OHP Workshop on Dwarf Galaxies, ed. G. Meylan & P. Prugniel (Garching: ESO), 13
Binney, J., & Tremaine, S. 2008, Galactic Dynamics (2nd ed.; Princeton, NJ: Princeton Univ. Press)
Block, D. L., Bournaud, F., Combes, F., Puerari, I., & Buta, R. 2002, A&A, 394, L35
Borriello, A., Salucci, P., & Danese, L. 2003, MNRAS, 341, 1109
Bournaud, F. 2016, ASSL, 418, 355
Bournaud, F., & Combes, F. 2002, A&A, 392, 83
Bournaud, F., Combes, F., & Semelin, B. 2005, MNRAS, 364, L18
Bournaud, F., Elmegreen, B. G., & Elmegreen, D. M. 2007, ApJ, 670, 237
Bournaud, F., Elmegreen, B. G., & Martig, M. 2009, ApJL, 707, L1
Brooks, A., & Christensen, C. 2016, ASSL, 418, 317
Busarello, G., Capaccioli, M., Capozziello, S., Longo, G., & Puddu, E. 1997, A&A, 320, 415
Cappellari, M., Bacon, R., Bureau, M., et al. 2006, MNRAS, 366, 1126
Cappellari, M., McDermid, R. M., Alatalo, K., et al. 2012, Natur, 484, 485
Cappellari, M., McDermid, R. M., Alatalo, K., et al. 2013a, MNRAS, 432, 1862
Cappellari, M., Scott, N., Alatalo, K., et al. 2013b, MNRAS, 432, 1709
Carollo, C. M. 1999, ApJ, 523, 566
Carollo, C. M., Stiavelli, M., de Zeeuw, P. T., & Mack, J. 1997, AJ, 114, 2366
Carollo, C. M., Stiavelli, M., Seigar, M., de Zeeuw, P. T., & Dejonghe, H. 2002, AJ, 123, 159
Chown, R., Li, C., Athanassoula, E., et al. 2019, MNRAS, 484, 5192
Ciotti, L., Lanzoni, B., & Renzini, A. 1996, MNRAS, 282, 1
Cleveland, W. S., & Devlin, S. J. 1988, J. Am. Stat. Assoc., 83, 596
Combes, F. 1996, in ASP Conf. Ser. 91, IAU Coll. 157: Barred Galaxies, ed. R. Buta, D. A. Crocker, & B. G. Elmegreen (San Francisco, CA: ASP), 286
Combes, F., Debbasch, F., Friedli, D., & Pfenniger, D. 1990, A&A, 233, 82
Combes, F., & Sanders, R. H. 1981, A&A, 96, 164
Costantin, L., Corsini, E. M., Méndez-Abreu, J., et al. 2018, MNRAS, 481, 3623
Costantin, L., Méndez-Abreu, J., Corsini, E. M., et al. 2017, A&A, 601, A84
Davies, R. L., Efstathiou, G., Fall, S. M., Illingworth, G., & Schechter, P. L. 1983, ApJ, 266, 41
de Jong, R. S. 1996, A&A, 313, 45
de Lorenzo-Cáceres, A., Méndez-Abreu, J., Thorne, B., & Costantin, L. 2019, MNRAS, 484, 665
de Vaucouleurs, G. 1948, AnAp, 11, 247
Djorgovski, S. 1987, in IAU Symp. 127, Structure and Dynamics of Elliptical Galaxies, ed. P. T. de Zeeuw (Dordrecht: Reidel), 79
Djorgovski, S., & Davis, M. 1987, ApJ, 313, 59
Djorgovski, S., de Carvalho, R., & Han, M.-S. 1988, in ASP Conf. Ser. 4, The Extragalactic Distance Scale, ed. S. van den Bergh & C. J. Pritchet (San Francisco, CA: ASP), 329
D'Onofrio, M., Cariddi, S., Chiosi, C., Chiosi, E., & Marziani, P. 2017, ApJ, 838, 163
D'Onofrio, M., Fasano, G., Moretti, A., et al. 2013, MNRAS, 435, 45
Dressler, A., Lynden-Bell, D., Burstein, D., et al. 1987, ApJ, 313, 42
Eliche-Moral, M. C., Balcells, M., Aguerri, J. A. L., & González-García, A. C. 2006, A&A, 457, 91

Eliche-Moral, M. C., Rodríguez-Pérez, C., Borlaff, A., Querejeta, M., & Tapia, T. 2018, A&A, 617, A113
Elmegreen, B. G., Bournaud, F., & Elmegreen, D. M. 2008, ApJ, 688, 67
Emsellem, E., Cappellari, M., Krajnović, D., et al. 2011, MNRAS, 414, 888
Erwin, P., Saglia, R. P., Fabricius, M., et al. 2015, MNRAS, 446, 4039
Faber, S. M. 1977, in Evolution of Galaxies and Stellar Populations, ed. B. M. Tinsley & R. B. Larson (New Haven, CT: Yale Univ. Obs.), 157
Faber, S. M., Dressler, A., Davies, R. L., Burstein, D., & Lynden-Bell, D. 1987, in Nearly Normal Galaxies. From the Planck Time to the Present, ed. S. M. Faber (New York: Springer), 175
Faber, S. M., & Jackson, R. E. 1976, ApJ, 204, 668
Faber, S. M., Tremaine, S., Ajhar, E. A., et al. 1997, AJ, 114, 1771
Fisher, D. B., & Drory, N. 2008, AJ, 136, 773
Fisher, D. B., & Drory, N. 2010, ApJ, 716, 942
Fisher, D. B., & Drory, N. 2016, ASSL, 418, 41
Fisher, D. B., Drory, N., & Fabricius, M. H. 2009, ApJ, 697, 630
Fragkoudi, F., Athanassoula, E., & Bosma, A. 2016, MNRAS, 462, L41
Fukugita, M., Shimasaku, K., & Ichikawa, T. 1995, PASP, 107, 945
Gadotti, D. A. 2008, MNRAS, 384, 420
Gadotti, D. A. 2009, MNRAS, 393, 1531
Gallagher, J. S., Goad, J. W., & Mould, J. 1982, ApJ, 263, 101
Gao, H., & Ho, L. C. 2017, ApJ, 845, 114
Gao, H., Ho, L. C., Barth, A. J., & Li, Z.-Y. 2018, ApJ, 862, 100
Gao, H., Ho, L. C., Barth, A. J., & Li, Z.-Y. 2019, ApJS, 244, 34
Genzel, R., Burkert, A., Bouché, N., et al. 2008, ApJ, 687, 59
Gott, J. R., III 1977, ARA&A, 15, 235
Grosbøl, P., Patsis, P. A., & Pompei, E. 2004, A&A, 423, 849
Ho, L. C., Li, Z.-Y., Barth, A. J., Seigar, M. S., & Peng, C. Y. 2011, ApJS, 197, 21
Hopkins, P. F., Bundy, K., Croton, D., et al. 2010, ApJ, 715, 202
Hopkins, P. F., Cox, T. J., Younger, J. D., & Hernquist, L. 2009a, ApJ, 691, 1168
Hopkins, P. F., Somerville, R. S., Cox, T. J., et al. 2009b, MNRAS, 397, 802
Huang, S., Ho, L. C., Peng, C. Y., Li, Z.-Y., & Barth, A. J. 2013a, ApJ, 766, 47
Huang, S., Ho, L. C., Peng, C. Y., Li, Z.-Y., & Barth, A. J. 2013b, ApJL, 768, L28
Huang, S., Ho, L. C., Peng, C. Y., Li, Z.-Y., & Barth, A. J. 2016, ApJ, 821, 114
Illingworth, G. 1977, ApJL, 218, L43
Immeli, A., Samland, M., Gerhard, O., & Westera, P. 2004, A&A, 413, 547
Inoue, S., & Saitoh, T. R. 2012, MNRAS, 422, 1902
Izquierdo-Villalba, D., Bonoli, S., Spinoso, D., et al. 2019, MNRAS, 488, 609
Kaviraj, S. 2014, MNRAS, 440, 2944
Kent, S. M. 1985, ApJS, 59, 115
Kim, M., & Ho, L. C. 2019, ApJ, 876, 35
Kim, M., Ho, L. C., Peng, C. Y., Barth, A. J., & Im, M. 2017, ApJS, 232, 21
Kodaira, K., Watanabe, M., & Okamura, S. 1986, ApJS, 62, 703
Kormendy, J. 1977, ApJ, 218, 333
Kormendy, J. 1981, in The Structure and Evolution of Normal Galaxies, ed. S. M. Fall & D. Lynden-Bell (Cambridge: Cambridge Univ. Press), 85
Kormendy, J. 1982a, ApJ, 257, 75
Kormendy, J. 1982b, in Twelfth Advanced Course of the Swiss Society of Astronomy and Astrophysics, Morphology and Dynamics of Galaxies, ed. L. Martinet & M. Mayor (Sauverny: Geneva Obs.), 113
Kormendy, J. 1985, ApJ, 295, 73
Kormendy, J. 1987, in Nearly Normal Galaxies. From the Planck Time to the Present, ed. S. M. Faber (New York: Springer), 163
Kormendy, J. 1993, in IAU Symp. 153, Galactic Bulges, ed. H. Dejonghe & H. J. Habing (Dordrecht: Kluwer), 209
Kormendy, J. 2013, in Secular Evolution of Galaxies, ed. J. Falcón-Barroso & J. H. Knapen (Cambridge: Cambridge Univ. Press), 1
Kormendy, J. 2016, ASSL, 418, 431
Kormendy, J., & Barentine, J. C. 2010, ApJL, 715, L176
Kormendy, J., Byun, Y., Ajhar, E. A., et al. 1996, in IAU Symp. 171, New Light on Galaxy Evolution, ed. R. Bender & R. L. Davies (Dordrecht: Kluwer), 105
Kormendy, J., & Djorgovski, S. 1989, ARA&A, 27, 235
Kormendy, J., Drory, N., Bender, R., & Cornell, M. E. 2010, ApJ, 723, 54
Kormendy, J., & Fisher, D. B. 2008, in ASP Conf. Ser. 396, Formation and Evolution of Galaxy Disks, ed. J. G. Funes & E. M. Corsini (San Francisco, CA: ASP), 297
Kormendy, J., Fisher, D. B., Cornell, M. E., & Bender, R. 2009, ApJS, 182, 216
Kormendy, J., & Ho, L. C. 2013, ARA&A, 51, 511
Kormendy, J., & Illingworth, G. 1982, ApJ, 256, 460
Kormendy, J., & Illingworth, G. 1983, ApJ, 265, 632
Kormendy, J., & Kennicutt, R. C., Jr. 2004, ARA&A, 42, 603

Kroupa, P. 2001, MNRAS, 322, 231
Läsker, R., Greene, J. E., Seth, A., et al. 2016, ApJ, 825, 3
Lauer, T. R. 1985, ApJ, 292, 104
Lauer, T. R., Ajhar, E. A., Byun, Y.-I., et al. 1995, AJ, 110, 2622
Lauer, T. R., Faber, S. M., Gebhardt, K., et al. 2005, AJ, 129, 2138
Lauer, T. R., Gebhardt, K., Faber, S. M., et al. 2007, ApJ, 664, 226
Laurikainen, E., Salo, H., Buta, R., & Knapen, J. H. 2007, MNRAS, 381,
    401
Laurikainen, E., Salo, H., Buta, R., Knapen, J. H., & Comerón, S. 2010,
    MNRAS, 405, 1089
Li, Z.-Y., Ho, L. C., & Barth, A. J. 2017, ApJ, 845, 87
Li, Z.-Y., Ho, L. C., Barth, A. J., & Peng, C. Y. 2011, ApJS, 197, 22
Lin, L., Li, C., He, Y., Xiao, T., & Wang, E. 2017, ApJ, 838, 105
Lynden-Bell, D., Faber, S. M., Burstein, D., et al. 1988, ApJ, 326, 19
Méndez-Abreu, J., Aguerri, J. A. L., Corsini, E. M., & Simonneau, E. 2008,
    A&A, 478, 353
Méndez-Abreu, J., Aguerri, J. A. L., Falcón-Barroso, J., et al. 2018, MNRAS,
    474, 1307
Méndez-Abreu, J., Ruiz-Lara, T., Sánchez-Menguiano, L., et al. 2017, A&A,
    598, A32
Méndez-Abreu, J., Simonneau, E., Aguerri, J. A. L., & Corsini, E. M. 2010,
    A&A, 521, A71
Moore, B., Katz, N., Lake, G., Dressler, A., & Oemler, A. 1996, Natur,
    379, 613
Moore, B., Lake, G., & Katz, N. 1998, ApJ, 495, 139
Moore, B., Lake, G., Quinn, T., & Stadel, J. 1999, MNRAS, 304, 465
Neumann, J., Wisotzki, L., Choudhury, O. S., et al. 2017, A&A, 604, A30
Nieto, J.-L., Bender, R., & Surma, P. 1991, A&A, 244, L37
Noguchi, M. 1999, ApJ, 514, 77
Oklopčić, A., Hopkins, P. F., Feldmann, R., et al. 2017, MNRAS, 465, 952
Pahre, M. A., de Carvalho, R. R., & Djorgovski, S. G. 1998, AJ, 116, 1606
Paturel, G., Petit, C., Prugniel, P., et al. 2003, A&A, 412, 45
Peng, C. Y., Ho, L. C., Impey, C. D., & Rix, H.-W. 2002, AJ, 124, 266
Peng, C. Y., Ho, L. C., Impey, C. D., & Rix, H.-W. 2010, AJ, 139, 2097

Pfenniger, D. 1984, A&A, 134, 373
Pfenniger, D. 1985, A&A, 150, 112
Pfenniger, D., & Norman, C. 1990, ApJ, 363, 391
Poggianti, B. M., Jaffé, Y. L., Moretti, A., et al. 2017, Natur, 548, 304
Renzini, A. 1999, in The Formation of Galactic Bulges, ed. C. M. Carollo,
    H. C. Ferguson, & R. F. G. Wyse (Cambridge: Cambridge Univ. Press), 9
Renzini, A., & Ciotti, L. 1993, ApJL, 416, L49
Roberts, M. S., & Haynes, M. P. 1994, ARA&A, 32, 115
Rodriguez-Gomez, V., Sales, L. V., Genel, S., et al. 2017, MNRAS, 467, 3083
Sandage, A., Freeman, K. C., & Stokes, N. R. 1970, ApJ, 160, 831
Sauvaget, T., Hammer, F., Puech, M., et al. 2018, MNRAS, 473, 2521
Sellwood, J. A. 2014, RvMP, 86, 1
Sellwood, J. A., & Wilkinson, A. 1993, RPPh, 56, 173
Sérsic, J. L. 1968, Atlas de Galaxias Australes (Córdoba: Obs. Astron., Univ.
    Nac. Córdoba)
Shen, J., & Sellwood, J. A. 2004, ApJ, 604, 614
Simien, F., & de Vaucouleurs, G. 1986, ApJ, 302, 564
Tabor, M., Merrifield, M., Aragón-Salamanca, A., et al. 2017, MNRAS,
    466, 2024
Tonini, C., Mutch, S. J., Croton, D. J., & Wyithe, J. S. B. 2016, MNRAS,
    459, 4109
Toomre, A. 1977, in Evolution of Galaxies and Stellar Populations, ed.
    B. M. Tinsley & R. B. Larson (New Haven, CT: Yale Univ. Obs.), 401
Treu, T., Ellis, R. S., Liao, T. X., & van Dokkum, P. G. 2005, ApJL, 622, L5
Trujillo, I., Graham, A. W., & Caon, N. 2001, MNRAS, 326, 869
van den Bergh, S. 1976, ApJ, 203, 764
Wang, J., Hammer, F., Puech, M., Yang, Y., & Flores, H. 2015, MNRAS,
    452, 3551
Wang, J., Kauffmann, G., Overzier, R., et al. 2012, MNRAS, 423, 3486
Weinzirl, T., Jogee, S., Khochfar, S., Burkert, A., & Kormendy, J. 2009, ApJ,
    696, 411
Wyse, R. F. G., Gilmore, G., & Franx, M. 1997, ARA&A, 35, 637
Zhang, H., & Zaritsky, D. 2016, MNRAS, 455, 1364
Zhao, D., Ho, L. C., Zhao, Y., Shangguan, J., & Kim, M. 2019, ApJ, 877, 52